

**COMPUTATIONAL STUDY OF HYPERVELOCITY
IMPACTS ON METALLIC THERMAL PROTECTION
SYSTEMS**

By

Carl Caldwell Poteet

Bachelor of Mechanical Engineering,
University of Delaware, May 1996

A Thesis submitted to

The Faculty of

The School of Engineering and Applied Science
of the George Washington University in partial satisfaction
of the requirements for the degree of Master of Science

August 31st, 1998

This research was conducted at NASA Langley Research Center

Abstract

Hypervelocity impact resistance of metallic thermal protection systems (TPS) proposed for future reusable launch vehicles is an important design consideration. Metallic TPS will cover most of the surface of proposed future reusable launch vehicles. The foil gage metallic honeycomb sandwich that forms the outer surface of the TPS will be exposed to hypervelocity impacts from micrometeoroids and space debris while the vehicle is in low Earth orbit. Such hypervelocity impacts occur at velocities in excess of material sound speeds, and are capable of penetrating TPS and the substructure beneath. The response of an idealized TPS structure, consisting of an outer titanium honeycomb sandwich panel, a 5 cm gap, a titanium foil layer and an aluminum substructure, to an impact from an aluminum sphere is studied with the goal of developing more impact resistant metallic TPS concepts. Numerical simulations were performed using a multi-dimensional shock physics code to model a metallic TPS configuration for which experimental hypervelocity impact data was available. Seven axisymmetric models of an aluminum sphere impacting an idealized metallic TPS panel were generated as well as a single three dimensional model. Three axisymmetric models neglected the honeycomb core layer while studying the effect of computational cell size and the removal of the titanium foil layer. Four different models of honeycomb core were generated, two of which used a homogeneous layer of density equal to the average density of honeycomb core while the remaining models used axisymmetric tubes and rods to simulate discrete honeycomb core cell walls. The three dimensional model simulated impact of an aluminum sphere on a honeycomb sandwich panel with a square cell core. This model exactly accounted for panel geometry and was used as a reference. Experimental results were used in conjunction with the three dimensional model predictions to validate the axisymmetric models. Although honeycomb core simulations using homogeneous layers produced unsatisfactory results, axisymmetric core simulations compared favorably with three dimensional model predictions and experimental results.

Acknowledgments

I would like to thank the Thermal Structures Branch of NASA Langley Research Center for giving me the opportunity to conduct this research. I am most thankful for the guidance of my research advisor, Max Blosser, who always made time to discuss problems with me. I would like to thank Kim Bey and Kamran Daryabeigi for their advice and friendship. I also wish to thank my academic advisor, Dr. Robert Tolson of the George Washington University, for his helpful suggestions and enthusiasm.

I am most grateful for the modeling advice provided by Dr. Eugene Hertel of Sandia National Laboratories, and for being allowed access to Sandia's Teraflops Supercomputer.

Finally, I would like to thank my family, for the support they have always given me.

Table of Contents

Abstract	ii
Acknowledgments	iii
Table of Contents	iv
1 Introduction	1
2 Analysis	7
2.1 Problem Definition	7
2.2 Analytical Approach	7
3 Computational Results	19
3.1 Overview of Computational Results	19
3.1.1 Substructure Damage Mechanisms	19
3.1.2 <i>No H/C Core Model</i>	21
3.1.3 <i>No H/C Core, Titanium Foil Removed Model</i>	24
3.1.4 <i>No H/C Core, Coarse Mesh Model</i>	25
3.1.5 <i>Reduced Density H/C Core Model</i>	26
3.1.6 <i>Porous H/C Core Model</i>	27
3.1.7 <i>Cell Centered Impact Model</i>	28
3.1.8 <i>Junction Centered Impact Model</i>	30
3.1.9 3D Model Results	32
3.2 Correlation with Experimental Results (Hole Size Comparison)	38
3.3 Impulse Comparison	40
3.4 Axial Momentum Losses	49
3.5 Runtime	50
4 Conclusions	51
5 References	54

1 Introduction

The large space debris population poses a serious threat to orbiting vehicles. Space debris travels at orbital velocities, resulting in relative velocities of between 8 and 16 km/s when impact occurs with orbiting spacecraft. Since impact velocity will be in excess of material sound speeds, these impacts are classified as hypervelocity impacts. Space debris has many sources, including spacecraft deterioration, breakups, and intentionally discarded material. It consists largely of aluminum particles, as well as paint, electronic components, composites, titanium and steel.¹

Metallic Thermal Protection Systems (TPS) are candidates for use on future Reusable Launch Vehicles (RLV). Forming the exterior layer of an RLV, TPS will be exposed to impacts with space debris. Impacts may damage TPS and compromise its function of protecting the vehicle from aerodynamic heating. If the TPS is penetrated, there is the risk that the substructure beneath will be damaged, and possibly penetrated.

The metallic TPS studied in this paper is comprised of a metallic box encapsulating lightweight internal insulation². The configuration of a single panel is shown in Figure 1. The outer surface of the box is an Inconel 617 (will be referred to as inconel) honeycomb sandwich, the lower surface is a titanium 6-4 (will be referred to as titanium) cutout honeycomb sandwich panel, and the sides are corrugated inconel foil. The cutout honeycomb sandwich panel is a sandwich panel in which the honeycomb core and inner foil in the center of the panel are machined away to reduce weight.

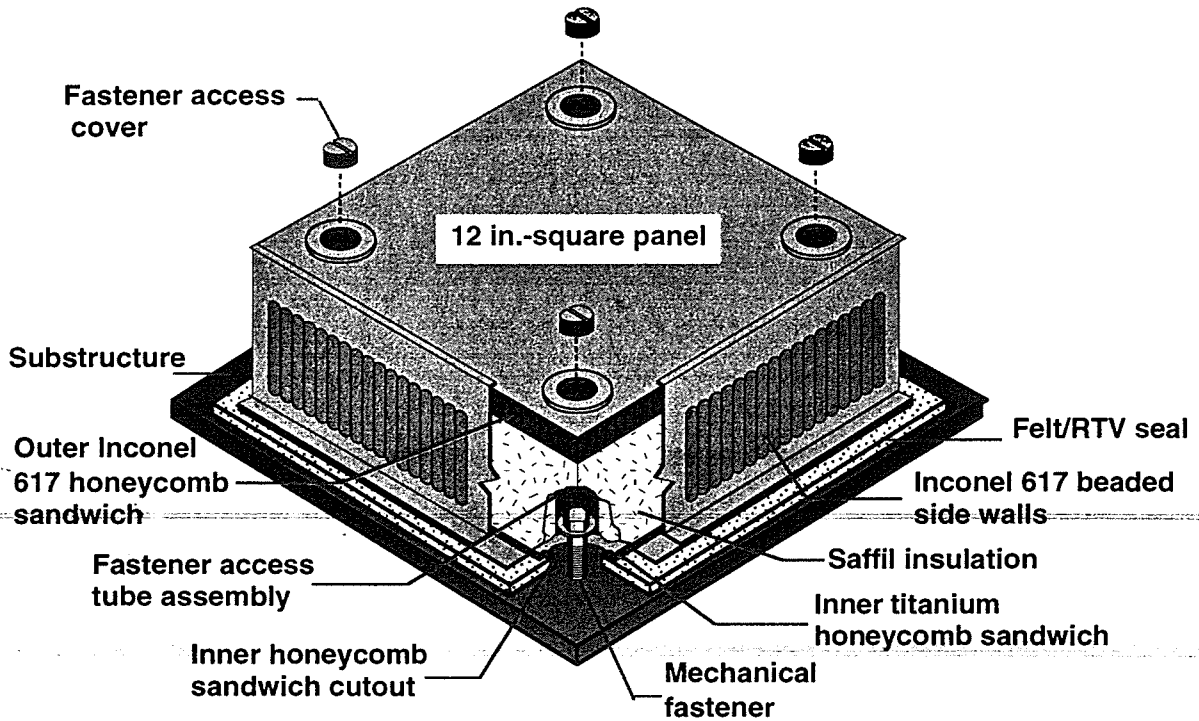


Figure 1. TPS Configuration

The metallic TPS configuration shown in Figure 1 has the potential to act as a hypervelocity impact shield (Whipple bumper shield). The Whipple bumper shield consists of one or more thin outer sacrificial shields in front of the structure to be protected (substructure). TPS has a structure similar to a Whipple shield, consisting of several foil layers exterior to the thicker substructure. During impact with a Whipple shield, large impact pressures are generated when the hypervelocity particle makes contact with the sacrificial outer shields, causing the particle to shatter and vaporize. The particle will form an expanding debris cloud as it penetrates through the Whipple shield. Upon impact with the substructure, particle momentum will be spread over a larger area than if it was intact, significantly reducing the danger of substructure penetration.

The effectiveness of Whipple shields is largely velocity dependent, since increased velocity will result in larger impact pressures. The influence of impact velocity is shown in Figure 2, which shows a conceptual ballistic limit for a Whipple shield. The critical diameter

represents the diameter of particle necessary to just penetrate the substructure, where any diameter below this diameter would be resisted by the substructure. Four different penetration regimes can be identified: Rigid Penetration, Shatter, Melting and Vaporization. Figure 2 does not report actual values, since critical diameter and the velocities at which different impact regimes occur will be dependent on the particle and shield materials. At relatively low impact velocities, less than ~ 4 km/s for an all aluminum particle and shield³, incoming particles will remain intact upon penetration of the outer Whipple shield layers, producing a significant threat to the substructure. This is known as Rigid Penetration. As impact velocity is increased, the particle will shatter upon contact with the outer foil layer, producing multiple fragments. Fragment size will decrease with increased velocity, reducing the risk of substructure penetration. This regime is known as the shatter regime. As impact velocity is further increased, melting and then vaporization will occur. Eventually, the impact velocity will be great enough that, even though the particle has been shattered and is in a liquid or gaseous state, the critical diameter will decrease. This increase in critical diameter occurs between 5.7 and 6.9 km/s for an all aluminum particle and shield.³

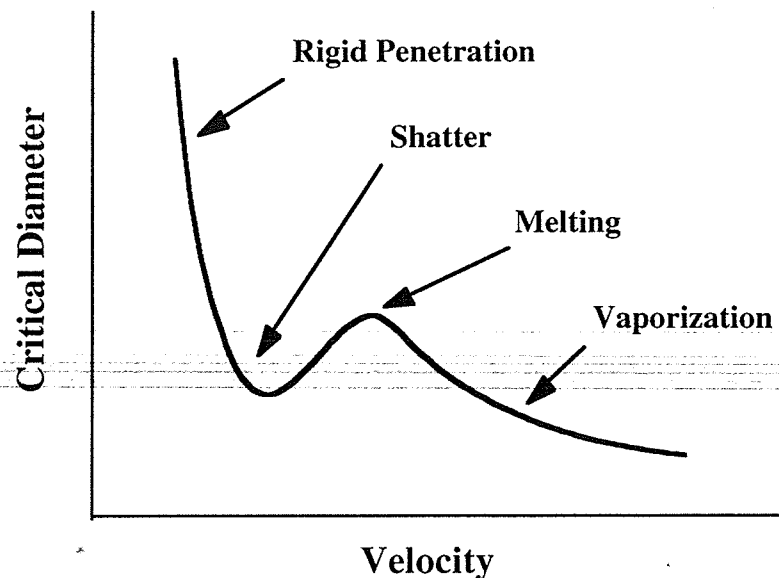


Figure 2. Conceptual Ballistic Limit for Impact on Whipple Shield.

The research described in this thesis represents part of an ongoing study at NASA Langley to develop a basis to design metallic TPS with improved resistance to hypervelocity impact. Previously, a series of 33 experimental hypervelocity impact tests were performed on metallic TPS by Katherine Karr⁴ using the facilities of NASA Marshall Space Flight Center Orbital Debris Simulation Facility. In these tests, the following parameters were investigated: facesheet material, facesheet thickness, cell size, thickness of insulation, and projectile diameter. During these tests, impact velocity was set at between 7 and 8 km/s, which represented the upper velocity attainable by the test facilities. Aluminum 1100-O projectiles of 0.3175 cm, 0.476 cm and 0.635 cm diameter were used. Two different facesheet materials were tested, inconel and titanium. The effect of facesheet thickness was investigated by varying inconel foil thickness from 0.00635 cm to 0.0254 cm and titanium foil thickness from 0.0076 cm to 0.036 cm. Inconel outer honeycomb panels were tested with both 0.476 cm and 0.635 cm honeycomb cell size, while titanium panels were tested with 0.476 cm cell size only. For the baseline configuration a 2 inch layer of lightweight fibrous insulation (Saffil), and a 0.00762 cm thick titanium foil layer behind the insulation layer was used to simulate the inner portion of the TPS panel. In all cases, a 0.254 cm thick 2024-T81 aluminum substructure was used. Substructure damage from the 0.3175 cm diameter projectile was very slight, ranging from no penetration to pinhole size penetration. Damage from the 0.476 cm projectile produced a wide range of substructure penetration, from pinhole size to 1.2 cm diameter holes. The large 0.635 cm diameter projectile in all cases resulted in massive damage to the substructure. Substructure hole diameters were in excess of 1.2 cm, and bulging of the substructure was evident in several experiments. From these results, it can be seen that the range of projectile sizes studied, at a velocity of around 8 km/s, represent the projectile sizes that are significant when it is wished to shield the substructure from a single impact. The small 0.3175 cm particle represents the smallest particle which is likely to penetrate the TPS and substructure, and in all tests with the large 0.635 cm particle massive substructure holes were

formed. The test data indicates that the largest projectile that could be adequately shielded against was the 0.476 cm diameter particle at an impact velocity of 7.1 km/s.

The purpose of this study is to develop a numerical simulation of a hypervelocity impact with metallic honeycomb sandwich panels, and to use it in a larger simulation of the entire TPS configuration. A shock physics code known as CTH⁵ was used to simulate the impact. A single experimental configuration was chosen for analysis due to runtime limitations. This configuration, shown in Figure 3, consisted of a 0.476 cm projectile, 0.0127 cm thick titanium facesheets, 2 inches of insulation, a third 0.00762 cm titanium foil layer behind the insulation, and a 0.254 cm thick aluminum substructure. Impact of the projectile was normal to the TPS panel. A 0.476 cm diameter projectile was studied for two reasons. From the experimental test data, it was clear that the 0.476 cm projectile was the largest that could be effectively shielded by TPS without drastically increasing system weight. For the 0.476 cm projectiles, substructure damage was very sensitive to TPS configuration, ranging from a pinhole sized penetration to a large hole.

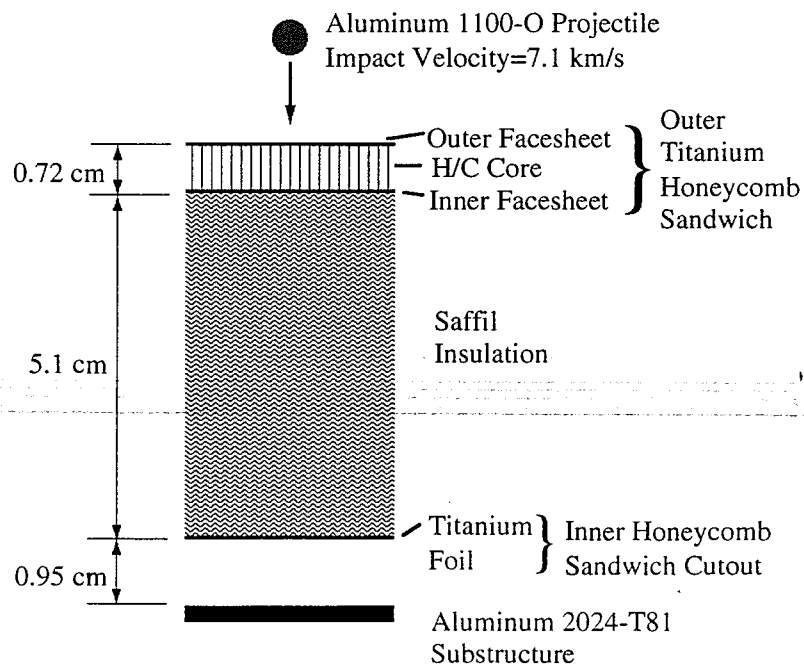


Figure 3. Schematic of TPS Configuration used in Computational Analysis

Seven different axisymmetric models were developed, three of which neglect the honeycomb core. The other models simulated the honeycomb core as either a homogeneous layer or discrete axisymmetric structures. In addition, a single three dimensional model was generated to determine the accuracy of the axisymmetric models. In the future, an axisymmetric model developed in this research will be used in a series of numerical simulations to develop a more impact resistant metallic TPS configuration.

2 Analysis

This chapter outlines the specific problem studied and the analytical approaches used in this research. Assumptions made during analysis are identified and discussed.

2.1 Problem Definition

For simplicity, this study considered the impact of a particle normal to the center region of a TPS panel and away from any edges or fasteners. The problem could then be simulated using an axisymmetric model. A cutaway view of the idealized TPS impact is shown in Figure 3. A particular configuration, corresponding to one of the tests in reference 4, was selected for analysis. The impacting particle was an aluminum 1100-O sphere of 4.76 mm diameter with an impact velocity of 7.1 km/s. This particle size was chosen to represent the largest particle which can be practically resisted by TPS without dramatically increasing the TPS weight. The outer honeycomb sandwich consisted of outer and inner facesheets of 0.127 mm thick titanium. The honeycomb core was made of 0.038 mm thick titanium. Honeycomb cells were square, with a 4.76 mm cell size and 7.2 mm core width. A total of 51 mm of Saffil fibrous insulation was contained between the outer and inner honeycomb sandwiches. The inner honeycomb sandwich consisted of only a single layer of titanium 6-4 foil in the central region of the TPS panel. Thickness of the titanium foil was 0.0762 mm. The substructure was composed of 2.54 mm thick 2024-T81 aluminum.

2.2 Analytical Approach

The following section describes the analysis tool and modeling techniques used. Material modeling considerations and a detailed description of each model generated are also presented.

2.2.1 CTH Hydrodynamics Code

Numerical simulations were conducted using CTH, a shock-physics code, also known as a hydrodynamics code. CTH uses a finite volume technique with Eulerian mesh to solve the conservation equations⁵:

$$\frac{\partial \rho}{\partial t} + \frac{\partial \rho v_i}{\partial x_i} = 0 \quad (1)$$

$$\frac{\partial v_i}{\partial t} + v_j \frac{\partial v_i}{\partial x_j} = f_i + \frac{1}{\rho} \frac{\partial \sigma_{ji}}{\partial x_j} \quad (2)$$

$$\frac{\partial e}{\partial t} + v_i \frac{\partial e}{\partial x_i} = f_i v_i + \frac{1}{\rho} \frac{\partial (\sigma_{ij} v_i)}{\partial x_j} \quad (3)$$

where equation (1-3) are the conservation of mass, momentum and energy equations, respectively. Only mechanical effects are considered. Electromagnetic, chemical and heat conduction effects are neglected.⁶ In these equations, standard indicial notation is used, with repeated indices representing summation. The symbols ρ , v_i , f_i , σ_{ij} , and e represent material density, velocity, external body forces per unit mass, the stress tensor, and specific total energy, respectively.

CTH is capable of modeling complex, multi-dimensional, multi-material problems, and is capable of simulating problems characterized by large deformations and strong shocks. Multiple materials and voids can be accounted for within a given computational cell, and fragments smaller than a computational cell can be simulated accurately.

2.2.2 Material Modeling

Material modeling in hydrocodes can be broken into three categories: volumetric response, resistance to distortion, and failure.⁶ Material volumetric response, or resistance to compression, is predicted using an equation-of-state (EOS). Of the three material modeling categories, volumetric response has the largest influence on hypervelocity impacts⁷. For this reason, highly detailed tabularized EOS are used with CTH that report pressure and energy as a

function of density and temperature. The EOS used are valid through the range of densities and temperatures experienced in a hypervelocity impact, and account for multiple material phase changes. Material resistance to distortion, or constitutive response, is known to be in general a second order effect at the pressures involved in hypervelocity impacts.⁷ This is because the impact pressure is many times in excess of material strength. For this reason, a simple elastic-plastic model with Von Mises yield surfaces was used for the hypervelocity projectile and outer TPS layers. The substructure was modeled using the more detailed Johnson-Cook viscoplastic model, since it was expected that impact pressure would be much lower in the substructure. Failure in tension was modeled using the standard CTH option in which tension is relieved by introducing a void into computational cells when the mean principal stress exceeds fracture strength.

Table I contains the EOS, yield strength and fracture strength values used. The SESAME⁸ aluminum EOS was used for both Al 1100-O and Al 2024-T81, with a density correction factor being used with Al 2024-T81 to account for the lower density due to alloying. A tabularized version of the ANalytical Equation Of State (ANEOS)⁹ of titanium 6-4 was used to model all of the TPS foil layers. Materials in Table I with a numeric entry under yield strength used an elastic-plastic model with Von Mises yield surface for material strength. The substructure was modeled using the Johnson-Cook viscoplastic model¹⁰ with default values for 2024-T351 aluminum, since no constitutive model was available for 2024-T81. Failure in tension was modeled using the standard CTH option in which tension is relieved by introducing a void into computational cells when the mean principal stress exceeds the fracture strength. The fracture strength for 2024 aluminum is estimated from known values for 2219 aluminum given by Hertel³. Fracture strength for titanium is derived from the dynamic flow stress reported by Babcock¹¹ multiplied by a factor of two, as suggested by Silling¹². It should be noted that values for fracture strength are only estimates, however, at the high pressures involved it is assumed that they will not have a large effect on the overall accuracy of the model.

Table I: CTH Material Parameters

Material	EOS	Yield Strength (MPa)	Fracture Strength (MPa)
1100-O Al	SESAME Aluminum	34 ¹³	-100 ³
2024-T81 Al	SESAME Aluminum	Johnson- Cook	-1500 ³ (est.)
Ti 6-4	ANEOS Ti alloy	880 ¹⁴	-2860 ^{11,12} (est.)

During a hypervelocity impact simulation, a large amount of low density gas is generated, which tends to dramatically increase computational run time and may lead to numerical difficulties. Therefore, to avoid computational problems, low density gas was removed in two ways. A continuously running gas filter was used to remove material with both density below 0.005 gm/cm³ and pressure below 0.1 MPa. Discarding material of such low density is assumed to have a negligible effect on the simulation. In some instances, it was necessary to use gas filters during the rezoning process (see 2.2.4) as well. In general, such filters were used to remove materials with density below 0.005 gm/cm³, regardless of pressure. However, in a few cases this level of filtering was not adequate to avoid numerical computation problems, and successively higher density levels were filtered, with the highest filter level of 0.5 gm/cm³ used in the *No H/C Core* Model (see 2.2.5) Unfortunately, in these instances the percentage momentum loss can be significant, and there is the possibility that the level of damage to the substructure will be underpredicted. These concerns will be addressed more fully in Section 3.4.

2.2.3 Computational Techniques

Axisymmetric models were divided into a rectangular mesh of computational cells. Each rectangular computational cell represents a toroid about the axis of symmetry. A symmetric boundary condition was imposed along the axis of symmetry, preventing mass, momentum, stress deviator, and energy fluxes through the axis of symmetry. Absorbing

boundary conditions were used along all other boundaries, allowing material to 'flow' out of the computational domain. The material layers were unrestrained. Since impact occurs at velocities in excess of material sound speeds, the conditions at the edge of a material layer will not influence the response during the initial microseconds of impact.

Cell dimensions could be varied along the axial and radial axis only. Good modeling practice requires at least four computational cells through the thickness of each layer^{7,15}. In addition, computational cells should be square in impacted areas and cell sizes varied gradually to insure an accurate numerical solution. Except where noted, these modeling practices were followed, which resulted in a very dense computational mesh when thin foil layers were modeled. In some cases, cell sizes were increased in the region between the inner facesheet and the titanium foil to increase computational efficiency. In these cases, computational cell sizes would then be reduced to account for the thin titanium foil layer and enlarged through the thicker substructure region. It was also necessary to use larger computational cells at the outer edges of the titanium foil layer to reduce the computational domain to a reasonable size. The computational mesh around the titanium foil layer used in the *Cell Centered Impact Model* is shown in Figure 4, where each box represents 100 computational cells (10 cells in the X direction by 10 cells in the Y direction). As can be seen, a large cell density is required in the vicinity of the titanium foil layer, with gradually increasing cell sizes before and after the foil.

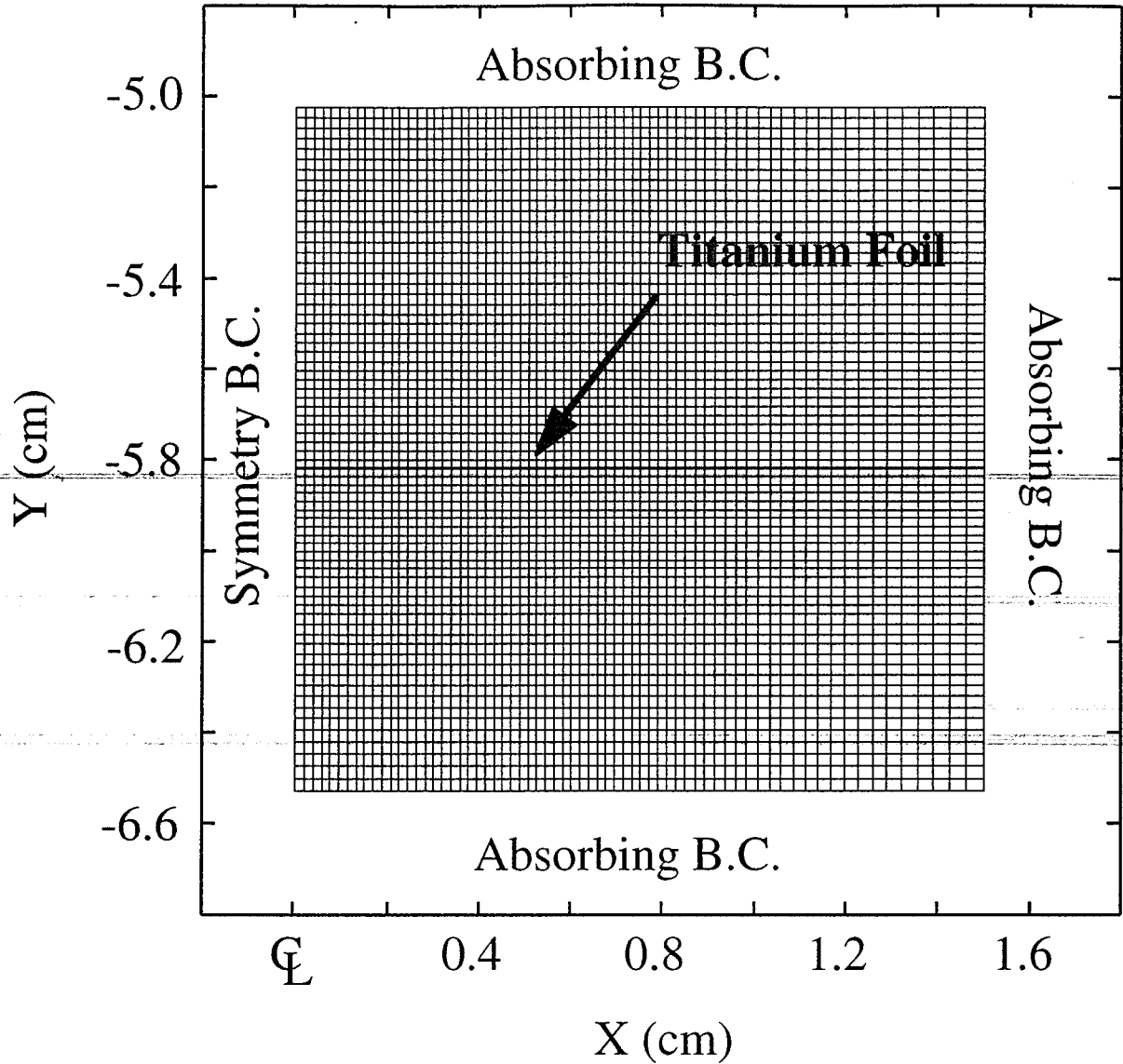


Figure 4. Meshing Scheme used to model Titanium Foil Impact in the *Cell Centered Impact Model*.

Very small computational cells were required in the vicinity of the thin foil layers to provide four computational cells through the wall thickness. Even though cell sizes were gradually increased away from walls, an overall model of the TPS would be too large to run on the IRIX workstations available. To overcome this limitation, two techniques were used. The first technique, used with all but one of the models, utilized numerous rezones. Calculation was initiated with a small region containing only the projectile and the honeycomb sandwich.

As the penetration proceeded and the debris cloud approached a boundary, the computation was rezoned, removing parts of the problem that no longer influenced the expanding debris cloud and adding more computational cells in front of the debris cloud as needed. At the appropriate location the titanium foil and substructure material layers were added. This procedure worked well, with between 11 and 15 rezones required for the overall simulation.

A second, more efficient, method was used with one of the models. This method uses a velocity addition routine contained in CTH which allows a uniform velocity field to be added to the computational mesh. By subtracting a velocity equal to the velocity of the center of mass of the debris cloud, the debris cloud can be held stationary while the mesh and material layers flow by it. The titanium foil and substructure were added by performing rezones. Also, several rezones were used to remove computational cells that no longer influenced the debris cloud and to filter low density material. Although this technique has many advantages, it was not developed until most of the simulations presented in the study had already been completed.

2.2.4 Models

Seven different axisymmetric models were made to simulate metallic TPS, as illustrated in Figure 5. Most models were similar, except in their treatment of the honeycomb core layer. Three models neglected the H/C core, two models treated the core as a homogeneous layer, and two other models incorporated discrete H/C cell walls. For simplicity, all of the models neglected the low density fibrous insulation layer. Although Saffil has only 1/80th the density of titanium, it will provide some resistance to the impact debris cloud. That benefit is neglected to make the analysis tractable. Simulations neglecting the insulation are assumed to predict conservative estimates of substructure damage.

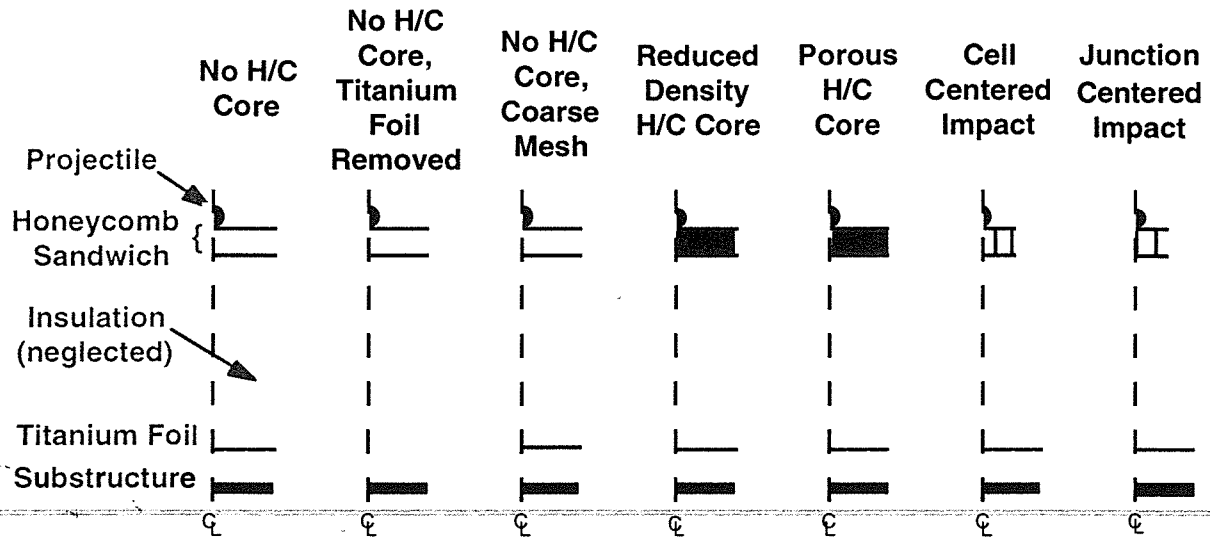


Figure 5. Overview of Axisymmetric Models

In addition to the axisymmetric models, a three dimensional model of the projectile and H/C sandwich was generated and run on Sandia National Laboratory's Intel Massively Parallel Computer, currently the world's fastest computer. Due to runtime and model size limitations, only the H/C sandwich could be modeled and the model was only run to 4 μ sec.

The *No H/C Core* Model accounted for only the outer facesheet, inner facesheet, titanium foil and substructure, omitting the honeycomb core layer. The 0.127 mm thick facesheets required that 0.03175 mm x 0.03175 mm computational cells (axial by radial) be used in the region around the outer honeycomb panel. The 0.076 mm foil comprising the titanium foil layer required that smaller 0.019 mm square computational cells be used in its vicinity. Near the substructure, computational cell size was increased to 0.019 mm x 0.03175 mm.

The small computational cell sizes necessary around the titanium foil layer required a significant amount of computational time. The *No H/C Core, Titanium Foil Removed* Model neglected the titanium foil to determine if it had a major influence on damage sustained by the substructure.

In the *No H/C Core, Coarse Mesh* Model, resolution was reduced to two computational cells through the thickness of a wall. The purpose of this model was to determine if the accuracy given by the recommended four cell resolution warranted the extra computational time required for such a detailed simulation.

The Reduced Density Honeycomb Core Model represents the first attempt at simulating honeycomb core. A homogeneous layer of reduced density titanium was inserted in between the outer and inner facesheet layers to account for the average mass of the honeycomb core. The same titanium constitutive and failure equations used to model the outer facesheet, inner facesheet and titanium foil layer were used in the modeling of the homogeneous layer. However, the EOS was modified with a density correction factor to account for the average density of the honeycomb core layer, which is approximately 1/59th that of solid titanium.

The Porous Honeycomb Core Model was a second attempt at using a homogeneous layer to represent honeycomb core. This model simulated the honeycomb as a porous material with density equal to 1/59th the density of solid titanium. A two state porosity model, also known as a snow-plow model, was used which modified the equation of state of the titanium layer. The initially porous material layer is allowed to compact in an irreversible process until reaching a non-porous state. At this point, the standard equation of state for titanium is used.

The *Cell Centered* and *Junction Centered Impact* Models used axisymmetric structures to represent the honeycomb core layer. One model represents a 4.76 mm diameter projectile impacting directly on the center of a honeycomb core cell (*Cell Centered Impact* Model) and the other model represents an impact occurring directly over a honeycomb core cell wall junction (*Junction Centered Impact* Model). These models are intended to bound the effect of impact location relative to the discrete honeycomb cells in the core. Figures 6 and 7 show the initial layouts of the honeycomb core region as portrayed in the cell centered and junction centered models, respectively. Y represents the axial dimension and X represents the radial dimension.

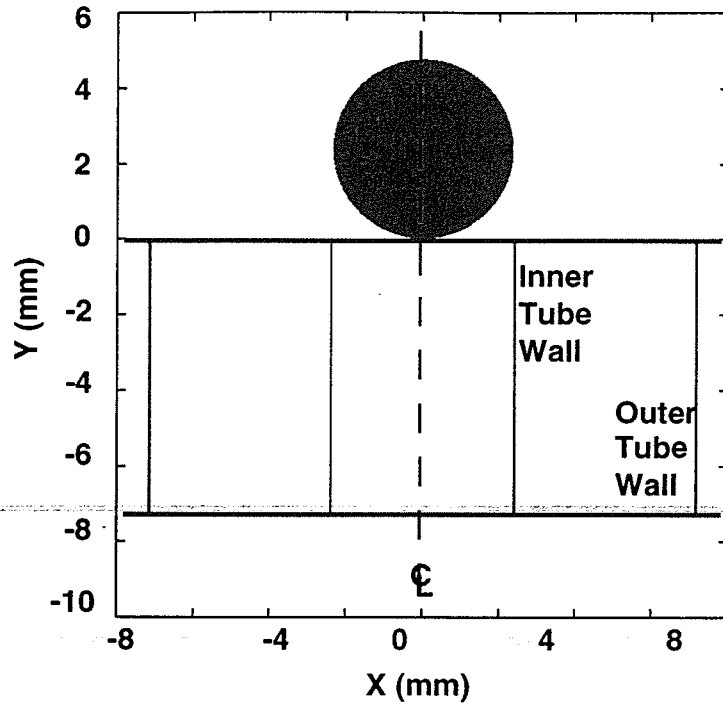


Figure 6. Initial Modeled Area of *Cell Centered Impact Model*

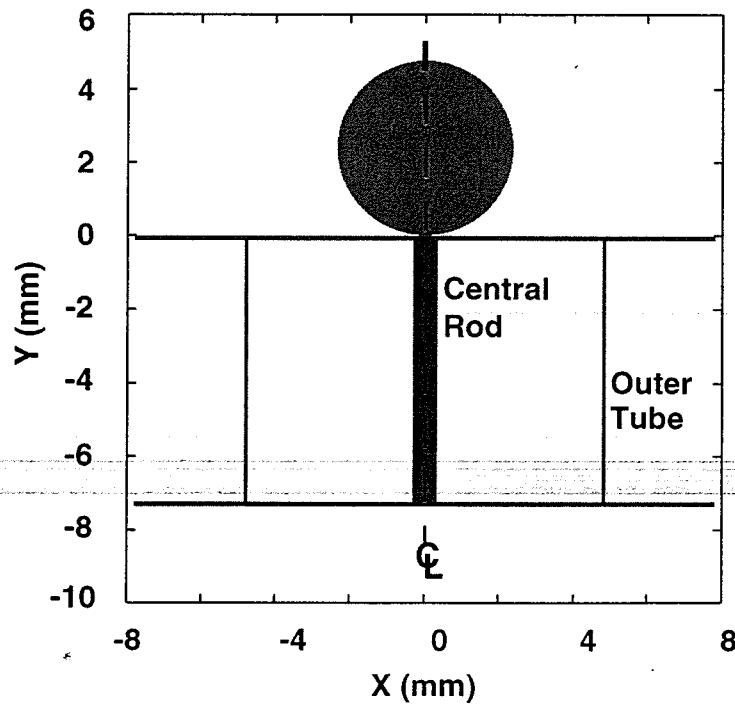


Figure 7. Initial Modeled Area of *Junction Centered Impact Model*

The discrete honeycomb core cells were simulated using axisymmetric tubes in the core. The diameters and wall thicknesses of these tubes were sized to have the same mass and similar mass distribution to the core being modeled. The inner tube for the *Cell Centered Impact* Model, with a diameter of 4.76 mm and thickness of 0.048 mm, was sized to have the mass of a single square honeycomb cell and diameter equal to the H/C cell size. The outer tube, with a diameter of 14.3 mm and a thickness of 0.08 mm, was sized to be inscribed in the box created by the eight square cells surrounding the innermost cell, with a mass equal to the mass of the walls of those eight cells, excluding walls shared with the innermost cell.

The *Junction Centered Impact* Model used similar axisymmetric tubes to simulate the discrete honeycomb cells. A central rod of 0.68 mm thickness was sized to equal the mass of honeycomb core contained in the path of the projectile. The second tube, with a diameter of 9.53 mm and wall thickness of 0.09 mm, was sized to represent the surrounding honeycomb cells.

The thin vertical walls present in the *Cell Centered* and *Junction Centered Impact* Models required smaller 0.012 mm square computational cells in the region around the honeycomb sandwich. In the model, the computational cell sizes were gradually increased after the inner facesheet, reaching a maximum size of 0.03175 by 0.02176 mm (y by x) midway between the inner facesheet and the titanium foil layer. Computational cell size was reduced to 0.01905 mm by 0.01905 mm near the titanium foil layer, and enlarged to 0.03175 mm by 0.03175 mm through the substructure.

The *Junction Centered Impact* Model made use of a velocity addition statement, which greatly simplified zoning. The initial mesh was composed entirely of 0.012 x 0.012 mm computational cells. Once calculation had proceeded past the inner facesheet, mesh size was increased to 0.01905 x 0.01905 mm. This size was maintained for the remainder of the calculation.

The 3D Model, as shown in Figure 8, was a quarter symmetry model which simulated the same problem as the axisymmetric models. A 3D rectangular mesh was used with symmetric boundary conditions imposed along the two planes of symmetry and absorbing boundary conditions along all other computational boundaries. Material properties and computational parameters were the same as for the axisymmetric models. Impact was simulated directly in the center of a square H/C core cell with a cell size of 0.475 cm. In addition to exactly modeling the geometry of the innermost square cell, the surrounding ring of cells were also modeled. Consistent with the actual TPS configuration, cell wall thickness was 0.0038 cm. To keep the overall model size within manageable limits, only two computational cells were used through the thickness of each wall. Care was taken to insure that cell size transition was smooth.

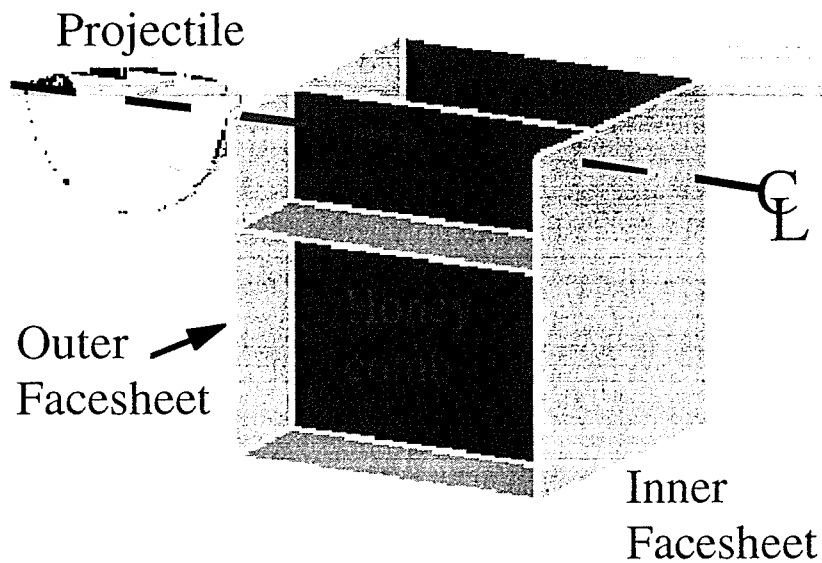


Figure 8. 3D Model Layout

3 Computational Results

The results generated by implementing the axisymmetric and 3D models discussed in Chapter 2 are presented in this chapter. Models are compared to each other based primarily on their prediction of substructure damage. In addition, computational results are compared to an experimental test on the basis of hole diameters in each of the material layers. Momentum losses resulting from rezoning are discussed and the runtime required for different models compared. Finally, the peak specific substructure impulses generated by the axisymmetric models are compared, and a comparison is made between the peak specific outer and inner foil impulses generated by the 3D and *Cell Centered Impact* Models.

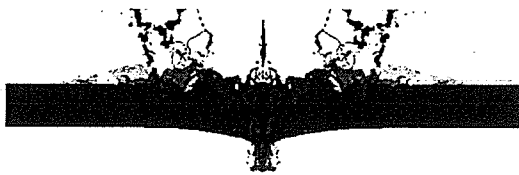
3.1 Overview of Computational Results

A description of the results generated using each of the models is given in this Section. Emphasis will be on the debris cloud structure as it penetrates the honeycomb sandwich layer and on the impact response of the substructure. Three characteristic damage mechanisms were observed in the substructure as it responded to impact with the debris cloud. These will be described in Section 3.1.1.

3.1.1 Substructure Damage Mechanisms

Substructure damage predicted using CTH fell into one of three categories: surface penetration and cratering, spalling, and momentum failure. These three failure mechanisms are illustrated in Figure 9, which shows the substructure failure predicted by the *No H/C Core*, *Cell Centered Impact*, and *Junction Centered Impact* Models, respectively. It is difficult to determine which quantities are important to surface penetration and cratering. Many different empirical equations have been derived to determine the penetration depth of a particle impacting a plate.^{1,16} These equations indicate a dependence on particle velocity and density, however there is not a direct, one-to-one dependence on momentum or kinetic energy. Spalling of large

areas is most likely due to the impulse generated from the liquid/gaseous portion of the debris cloud.¹ Lastly, momentum failure is due to the transfer of momentum from the debris cloud to the structure, where failure occurs by bulging or plugging. Momentum failure can be very sensitive to momentum distribution and momentum multiplication. Momentum multiplication is defined as the ratio of change in momentum of an impacted target over the pre-impact momentum of the impacting object. Gaseous debris will rebound elastically upon impact with the substructure, and has been assumed to produce a momentum multiplication of 2 in previous studies.¹ Cratering results in momentum multiplication due to ejection of debris from the impact crater in the direction opposite to the motion of the debris cloud.¹⁷ Momentum multiplication due to cratering may be as large as a factor of five.¹ In addition to momentum multiplication, surface damage and loading rate may be influential to momentum failure.¹



Penetration/Cratering:

- **Dependent on material velocity and mass**
- **No clear dependence on momentum or kinetic energy**



Spalling:

- **Due to impulse generated by liquid and gaseous portion of debris cloud**



Momentum Failure:

- **Results from transfer of momentum from the debris cloud to structure**
- **Very sensitive to momentum distribution and momentum multiplication**

Figure 9. Identified Substructure Failure Mechanisms

3.1.2 No H/C Core Model

The initial setup for the *No H/C Core Model* (Figure 5) consisted of only the projectile and the outer facesheet layer, with other layers added as the computation proceeded. Figure 10 shows the expanding impact debris cloud at several different times prior to substructure impact. The temperatures indicated on the color bar are the melting point (930 K) and vaporization temperature (2300 K) of aluminum¹⁸ at atmospheric pressure. This is to allow the state of the material to be estimated as the impact progresses. It can be seen that the outer foil layer, despite being much thinner than the projectile diameter, has shocked the projectile at 1.0 μsec , causing spalling to occur. Spalling is a tensile failure resulting from the reflection of compressive waves at free surfaces. The debris cloud is composed mostly of solid particles at this point.

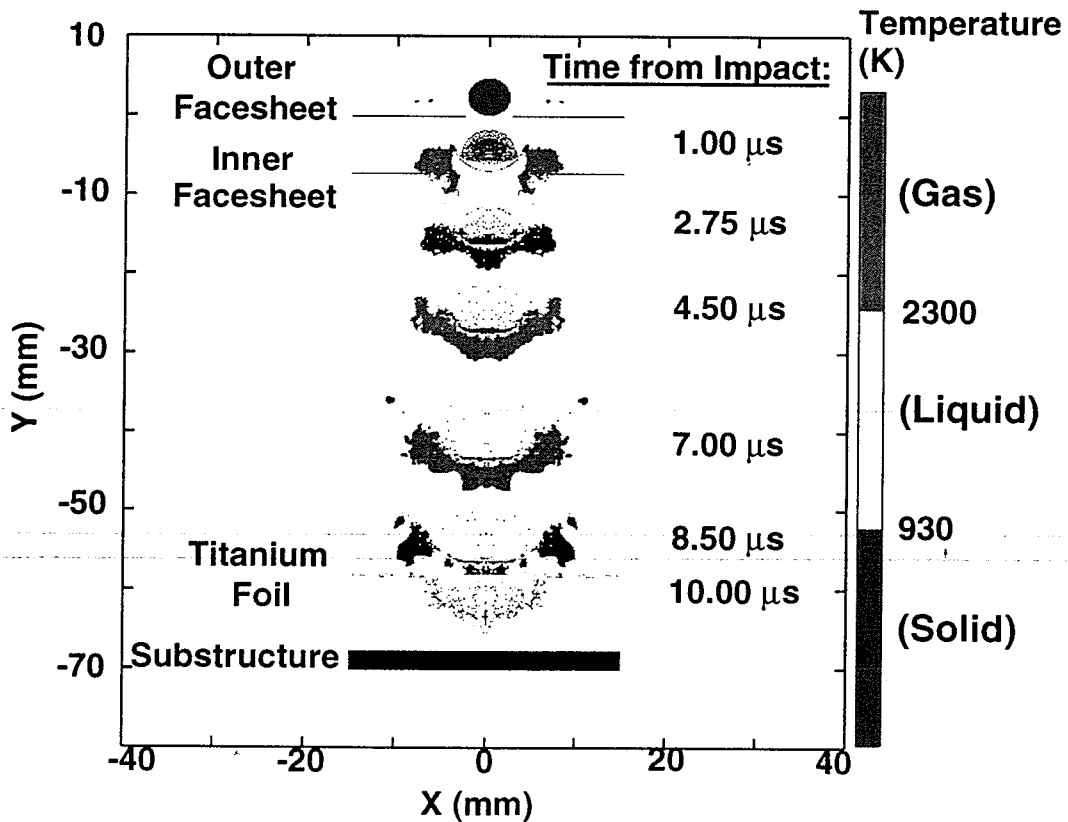


Figure 10. Time Elapsed View of TPS Penetration Predicted by *No H/C Core Model*

Upon impact with the second layer, the debris cloud was further shocked. At this time the leading edge of the debris cloud is composed of vaporous debris, with solid debris located at the center of the debris cloud. As the calculation progressed, mass accumulated along the axis of symmetry, forming a "spike" at the leading edge of the debris cloud (Figure 11). This is a common occurrence with axisymmetric models¹⁹. A particle directed toward the axis of symmetry will have radial velocity reduced to zero upon reaching it. The particle will still have an axial velocity component, resulting in the particle riding along the axis of symmetry. Mass accumulations of this type were seen in several models. In general, they were not altered. However, the spike in the *No H/C Core* Model was removed since computational difficulties resulted when it made contact with the titanium foil layer. Removal of the spike resulted in a 3% drop in downward axial momentum, that is, the momentum directed toward the substructure. The percentage drop is calculated relative to the initial, time zero, momentum in the system. The titanium foil layer was easily penetrated by the debris cloud, and a second axis of symmetry mass accumulation occurred prior to substructure impact. As can be seen in Figure 12 the dense mass accumulation results in the initial substructure penetration, causing a small diameter central penetration. By 15 μ sec., the rest of the debris cloud has generated a large diameter hole in the substructure, by the combined effect of cratering / penetration, spalling, and the absorption of the debris cloud momentum. Since axis of symmetry mass accumulations witnessed in other models were seen to produce damage only in a narrow region along the axis of symmetry, and since the entire central region in this model was penetrated, it is assumed that removal of the pre-titanium-foil-impact mass did not significantly influence the calculation.

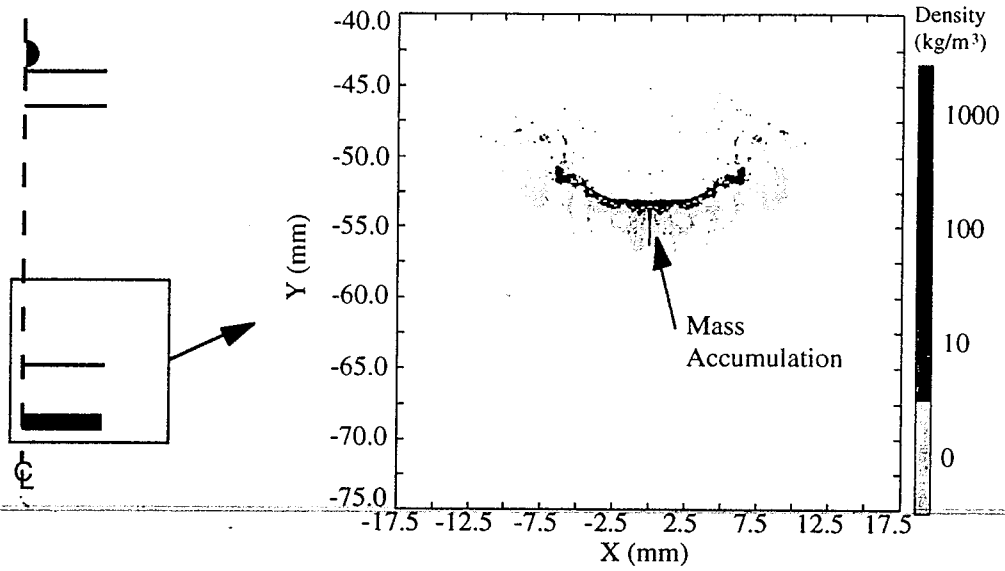


Figure 11. Axis of Symmetry Mass Accumulation in *No H/C Core Model* Prior to Titanium Foil Impact

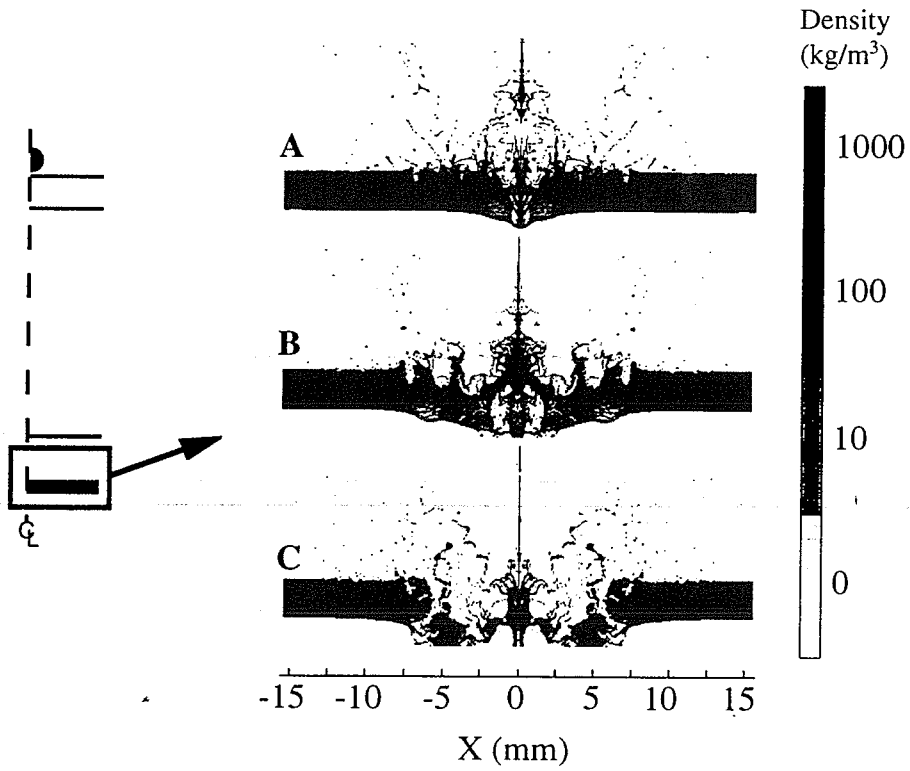


Figure 12. *No H/C Core Model* Substructure Penetration. A, B, and C Represent 11.4, 12.8, and 15.1 $\mu\text{sec.}$, Respectively.

3.1.3 *No H/C Core, Titanium Foil Removed Model*

A substantial amount of computational time was required to model penetration of the thin titanium foil layer. To assess the importance of the titanium foil layer, the *No H/C Core, Titanium Foil Removed Model*, identical to the *No H/C Core Model*, was generated without the titanium layer. The stages of substructure penetration are shown in Figure 13. The damage is qualitatively different from the damage observed in the *No H/C Core Model*. The primary damage mechanism is spalling to the rear of the specimen, instead of penetration and cratering. In addition, the substructure hole size generated without the titanium foil layer was substantially larger than the hole size predicted by the *No H/C Core Model*, 2.13 cm as opposed to 1.46 cm. Comparison with Figure 12 clearly shows the difference in damage predictions with and without the titanium foil layer, leading to the conclusion that the titanium foil layer is necessary to accurately predict substructure damage.

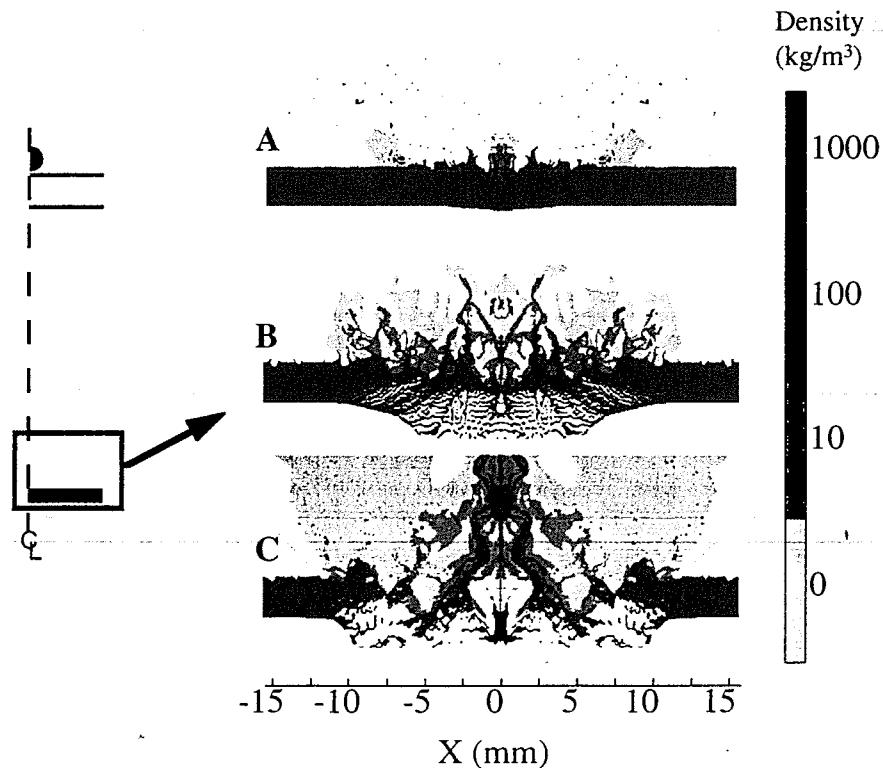


Figure 13. Substructure Penetration Predicted by *No H/C Core, Titanium Foil Removed Model*. A, B, and C Represent 11, 12, and 15 $\mu\text{sec.}$, Respectively.

3.1.4 *No H/C Core, Coarse Mesh Model*

The purpose of this model was to determine the effect of enlarging cell sizes by a factor of two in hopes of decreasing the computational time (~ 5 CPU days) required for a simulation. Instead of four cells through the thickness of walls, only two were used. Figure 14 shows the penetration of the outer and inner facesheet layers of the outer honeycomb sandwich. Qualitatively the debris cloud is similar to the debris cloud generated in the *No H/C Core Model*, composed largely of low density debris, with high density debris in the center of the cloud. Scattered high density particles are seen behind the high density central region, the result of spalling to the rear of the projectile as it impacted the outer facesheet layer.

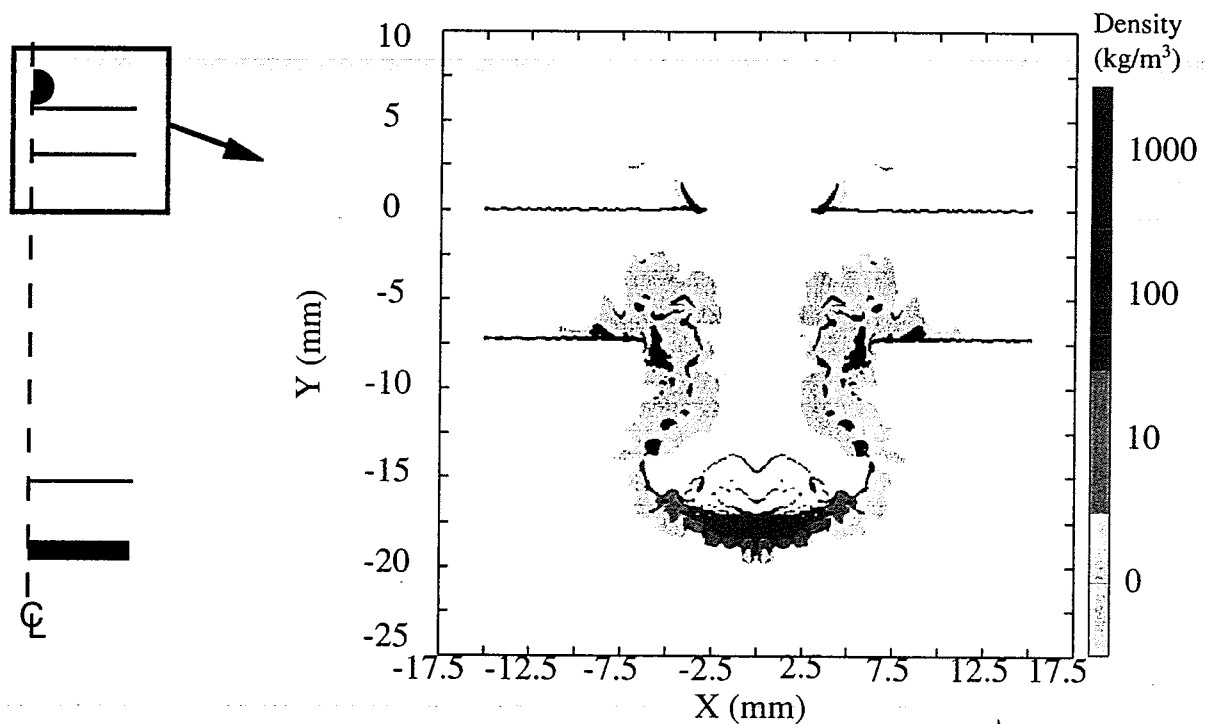


Figure 14. Penetration of Outer and Inner Facesheets Predicted by *No H/C Core, Coarse Mesh Model*. Results Shown at 3 μsec.

Substructure penetration was similar to the *No H/C Core Model* in many respects. As shown in Figure 15, there was a central penetration due to debris accumulated on the axis of symmetry. A larger penetration is caused by the combined effect of surface penetration and absorption of debris cloud momentum. There were two differences. There is no spalling to

the rear of the substructure, and upon failure there is a noticeable bulge in the substructure which was not present in the *No H/C Core* Model. However, runtime was reduced by a factor of 4.5, 1.03 CPU days instead of 4.62 CPU days, making the *No H/C Core, Coarse Mesh* Model more tractable for use in parametric studies.

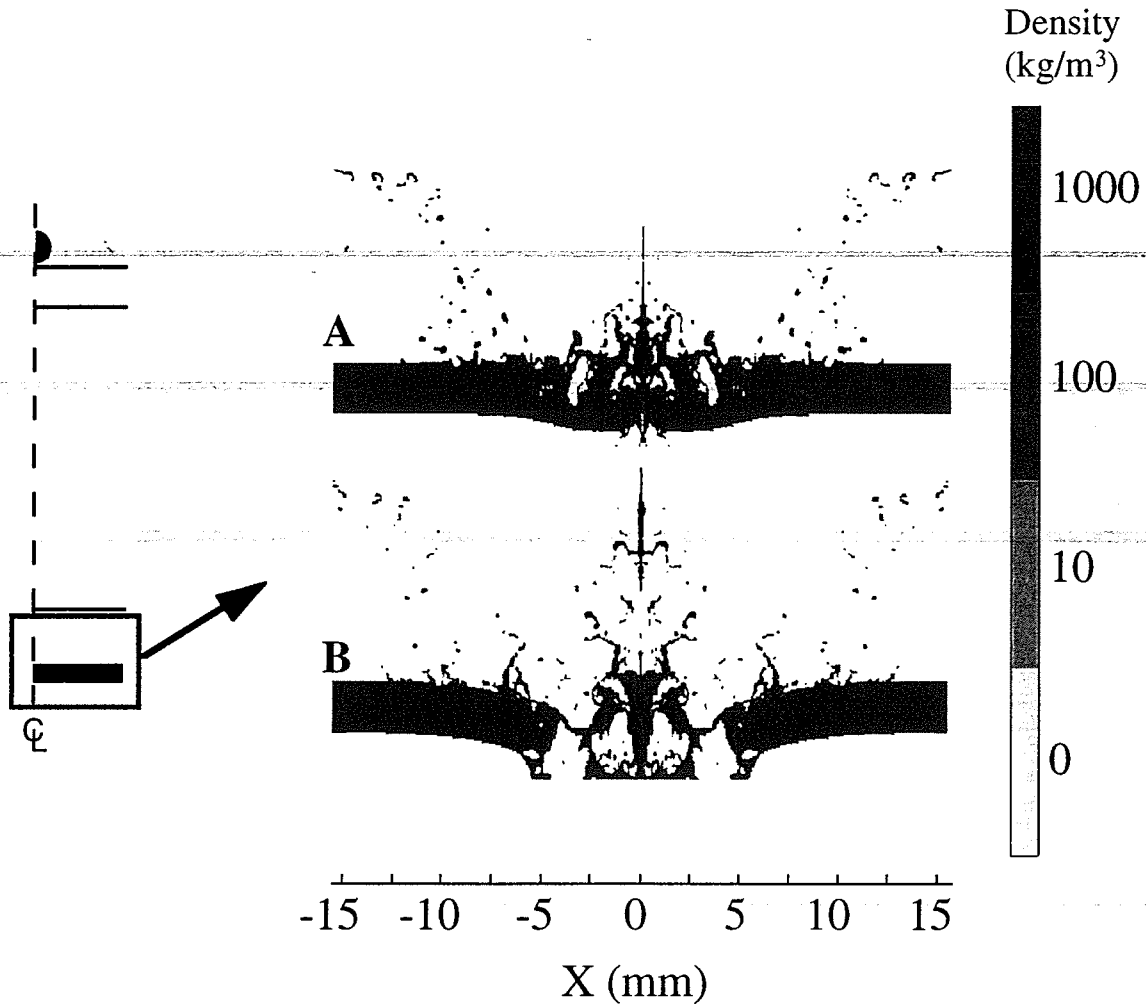


Figure 15. *No H/C Core, Coarse Mesh* Model Prediction of Substructure Penetration. A and B Represent 12.3 and 15.0 μ sec., Respectively.

3.1.5 *Reduced Density H/C Core* Model

This model was generated to simulate the honeycomb core as a homogeneous layer of reduced density. This method did not work well however, since reducing material density resulted in an increase in material sound speed. Material sound speed is proportional to the

square root of the inverse of material density, so using material with density reduced to 1/59th of its original density increases material sound speed by nearly a factor of eight. This resulted in a material sound speed several times in excess of projectile velocity, meaning that this model would not behave as a hypervelocity impact. This effect is shown in Figure 16, where the pressure wave in the honeycomb layer is traveling faster than the impacting projectile. Since the sound speed of titanium, 5.1 km/s, is less than the impact velocity of 7.1 km/s the model is clearly inaccurate. This unrealistic prediction resulted in the calculation being canceled.

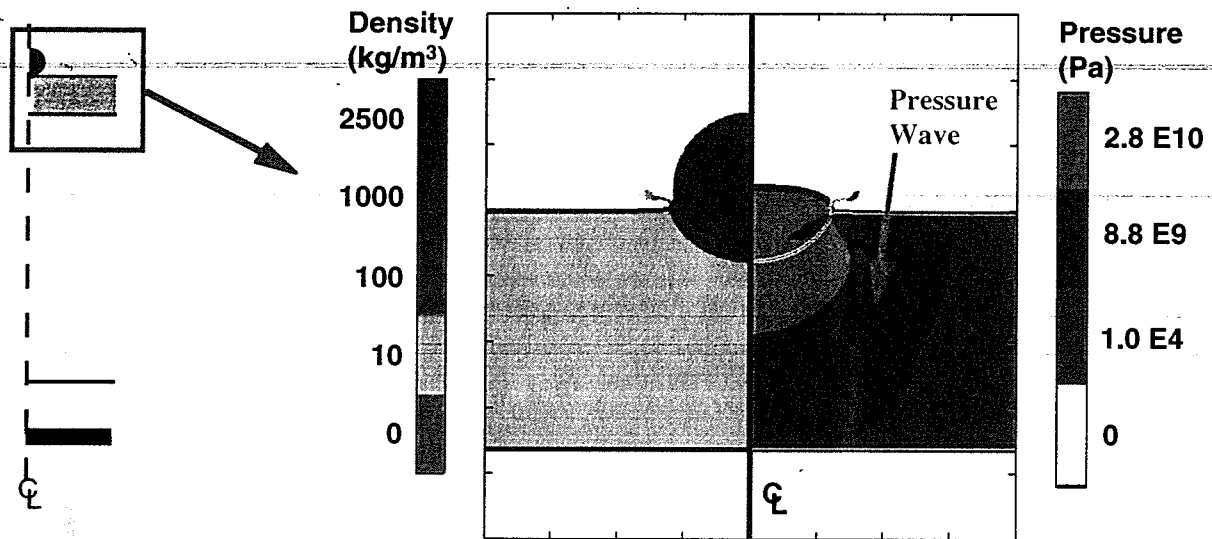


Figure 16. Reduced Density H/C Core Model at 0.125 μ sec. Low H/C Core Density Results in Unrealistic Material Sound Speed.

3.1.6 Porous H/C Core Model

The Porous H/C Model represents a second attempt of simulating honeycomb core with a homogeneous layer of material. This time an existing CTH porosity model was used. Although this corrected the speed of sound inaccuracies of the Reduced Density H/C Model, the predicted behavior of the debris cloud as it exited the inner foil layer did not appear realistic. In Figure 17, as the debris cloud moved away from the inner facesheet layer, dense debris from that layer moved outward with a velocity as high as 8.5 km/s. Honeycomb debris, still compressed by the initial impact at 2.25 μ sec., formed a rapidly expanding region of low

density materials between debris from the inner foil layer and the projectile. This prediction was not consistent with the predictions of models without H/C core, as shown in Figures 10 and 14, in which the inner facesheet and projectile debris remained joined after initial impact. Furthermore, it was not consistent with the prediction of the 3D Model, which will be discussed in Section 3.1.9. Because of its lack of correlation with other models, the Porous H/C Model was not run to completion.

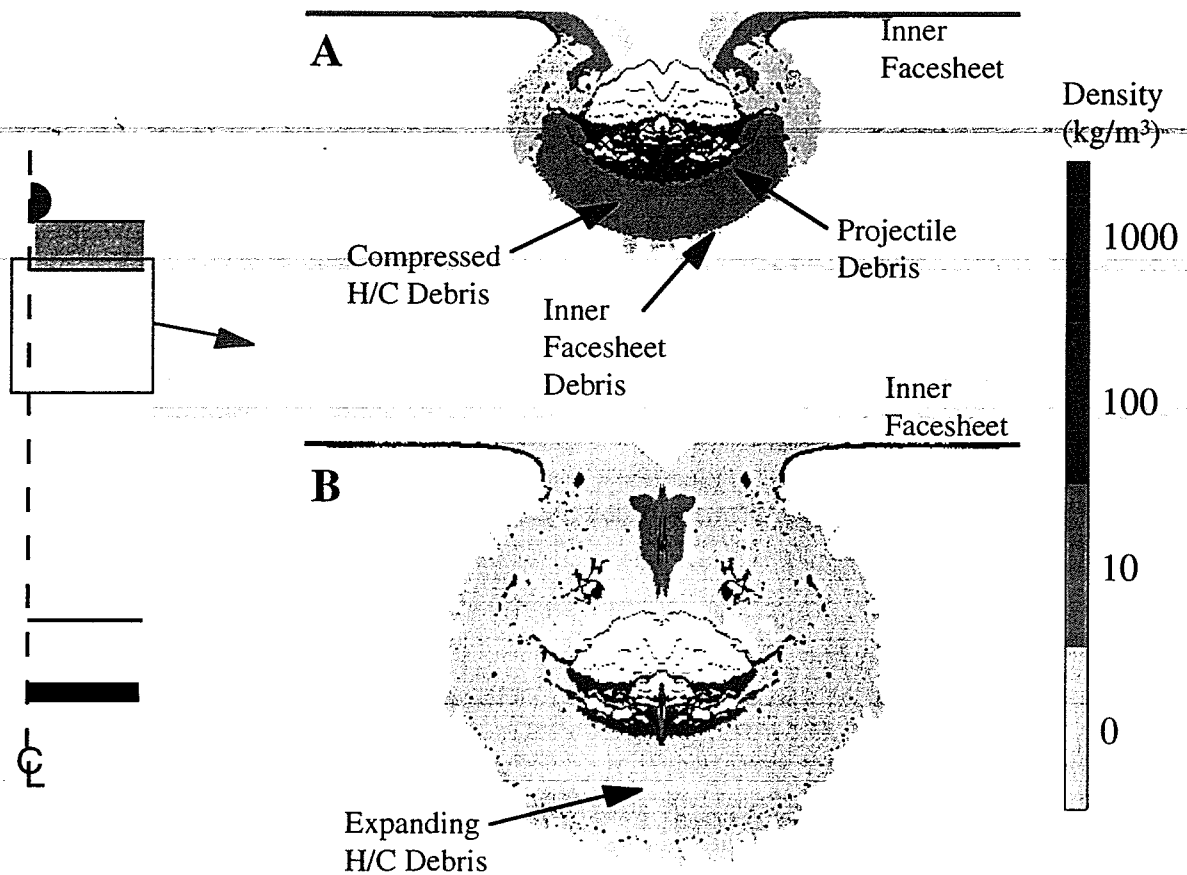


Figure 17. Porous H/C Core Model Predicting Unrealistic Debris Cloud Expansion. A and B Represent 2.25 and 3.13 μ sec., Respectively.

3.1.7 Cell Centered Impact Model

The initial layout of the *Cell Centered Impact Model* is shown in Figure 6. After impact with the outer facesheet layer spalling occurred in the projectile. The majority of debris was contained inside the inner tube. Figure 18 shows the predicted channeling effect. In the

process of channeling the impact debris cloud, the inner tube was destroyed. A large concentration of high density debris persisted to substructure impact, as shown in the top frame of Figure 19. This highly concentrated debris cloud penetrated the substructure, producing a large hole. Some spalling is also noticeable to the rear of the substructure, but it is not the predominant failure mechanism.

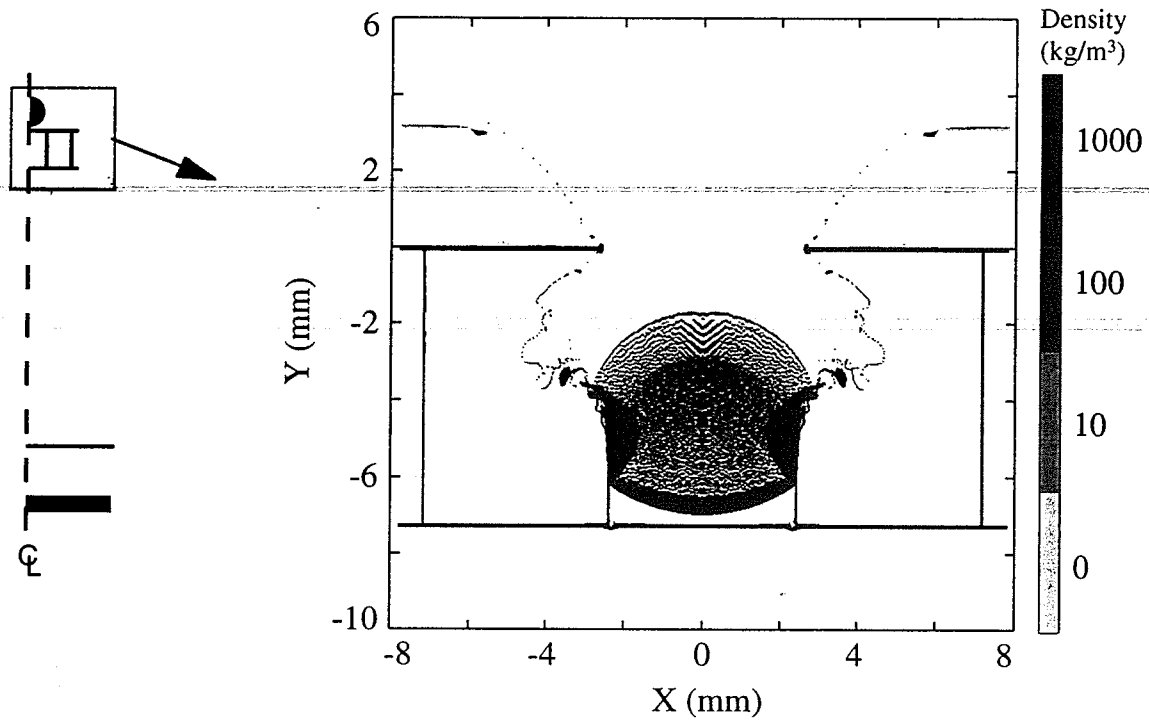


Figure 18. Channeling of Debris Cloud Predicted by *Cell Centered Impact Model*.

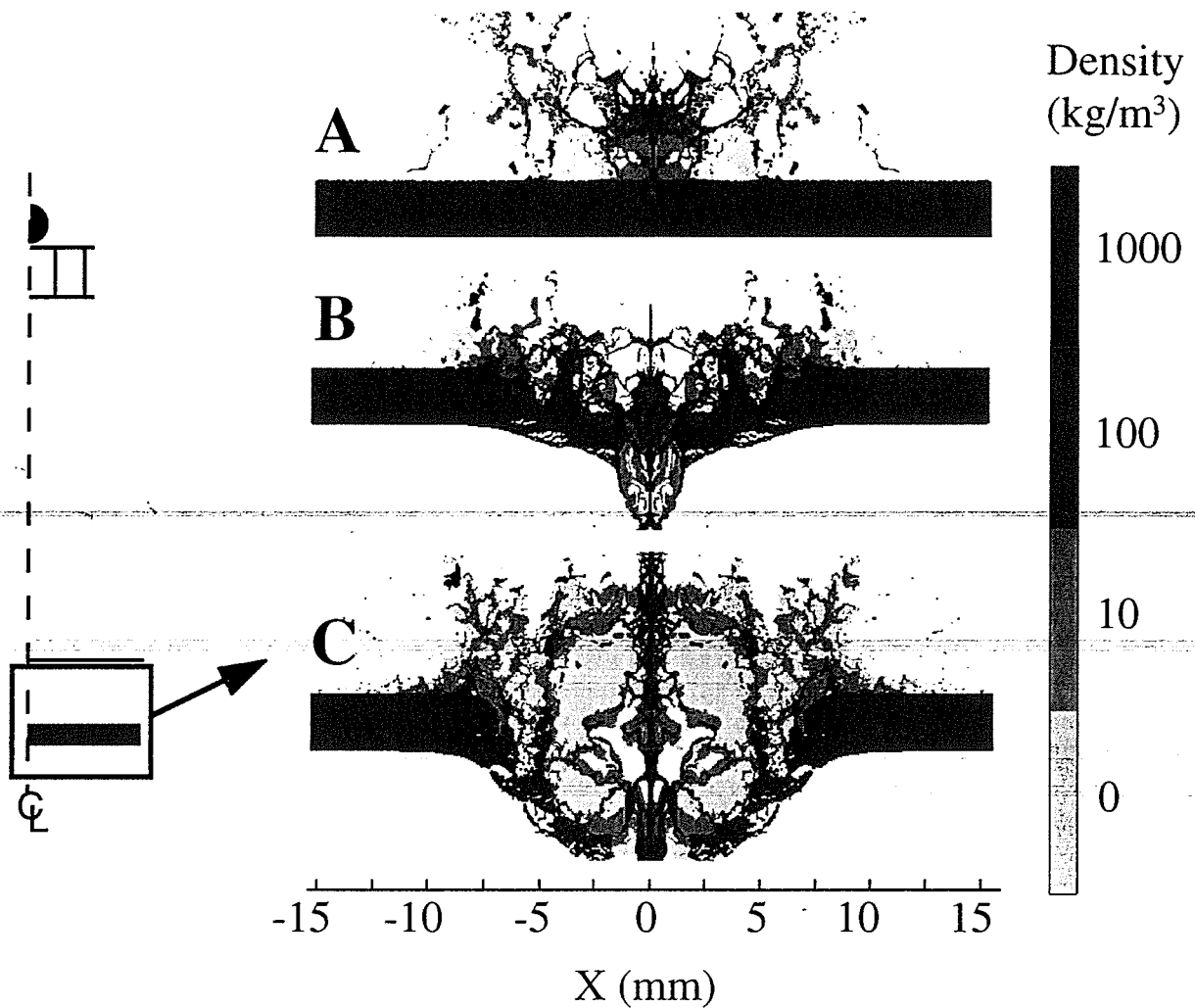


Figure 19. Substructure Penetration Predicted by *Cell Centered Impact Model*. A, B, and C Represent 11, 12 and 14 μ sec., Respectively.

3.1.8 *Junction Centered Impact Model*

The *Junction Centered Impact Model* was created to simulate an impact centered on the junction of the corner or four adjacent honeycomb cells. The initial layout is shown in Figure 7. As impact progressed past the outer facesheet layer, the debris cloud was deflected away from the axis of symmetry as the central rod was eroded, as shown in Figure 20. Spalling occurred toward the rear of the projectile. The debris cloud continued to diverge as it progressed through the inner facesheet and titanium foil layers. As seen in Figure 21, upon reaching the substructure the debris cloud density is not concentrated in the center as it was for

the *Cell Centered Impact Model*. Initial failure was due to mass concentrated along the axis of symmetry, resulting in a small diameter hole. Late time failure appears to be due to “plugging”, in which the momentum from the debris cloud absorbed by the substructure results in failure of the substructure by shear. As it failed, the central portion of the substructure was pushed out.

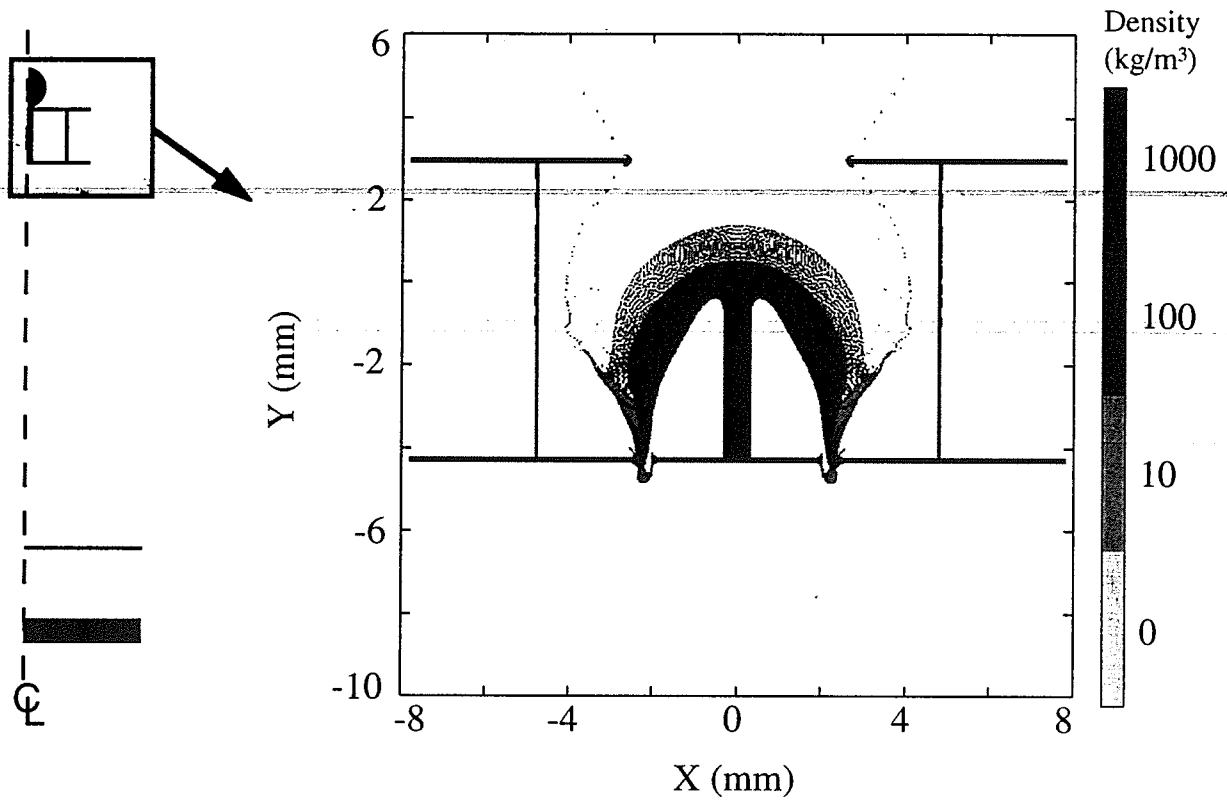


Figure 20. Junction Centered Impact Model Prediction of Honeycomb Penetration.

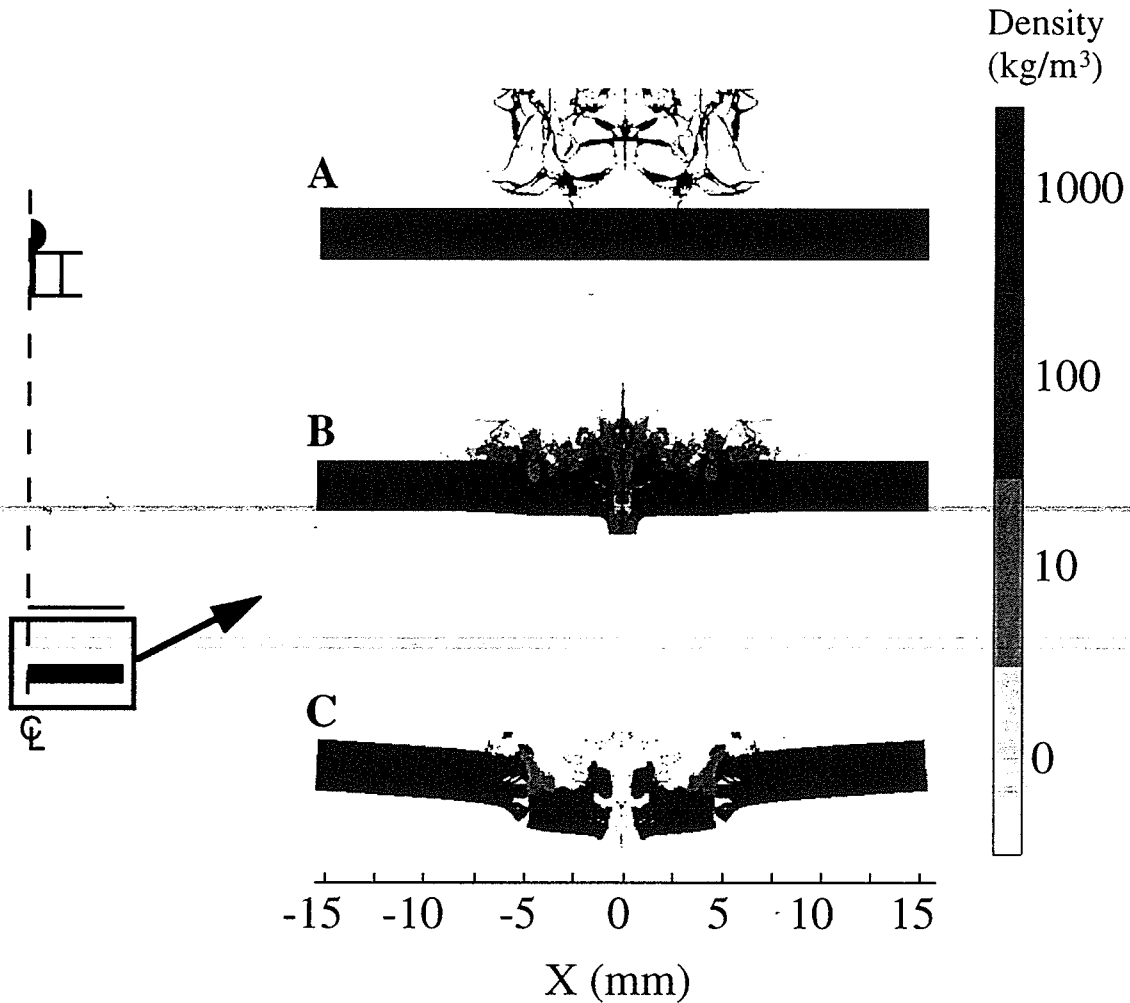


Figure 21. Substructure Penetration Predicted by *Junction Centered Impact Model*. A, B, and C Represent 9.6, 11.0, and 20.0 $\mu\text{sec.}$, Respectively.

3.1.9 3D Model Results

The 3D Model represents the best computational approximation available with current computational limitations. Therefore, by comparing it to the axisymmetric *Cell Centered Impact Model* the validity of using axisymmetric models can be determined.

Figures 22 and 23 show a three dimensional perspective of material locations at 1 and 2 $\mu\text{sec.}$, respectively. The 3D Model predicts that the innermost honeycomb cell will contain the impact debris cloud to a large extent, being destroyed in the process. In Figure 23, the debris

cloud is seen to emerge from the rear of the H/C sandwich in a concentrated mass, roughly the shape of the inner cell.

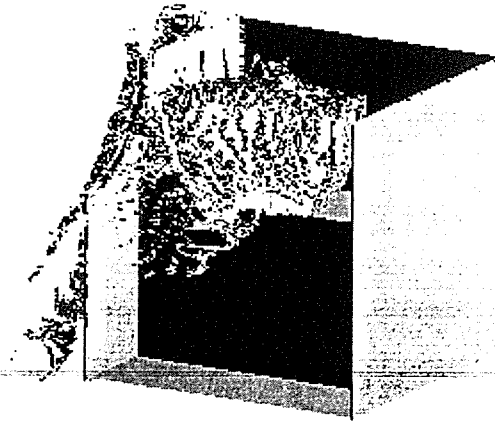


Figure 22. 3D Simulation at 1 μ sec.



Figure 23. 3D Simulation at 2 μ sec.

Figures 24 and 25 compare the density distributions obtained with the axisymmetric model and the 3D Model at 1 and 2 μ sec., respectively. Results from the 3D Model are shown along the plane of symmetry, so that comparison can be made with the axisymmetric model. Both models predict that the inner honeycomb cell will channel the debris cloud, as can be seen in Figure 24. In addition, the shape of the dense region ($> 1000 \text{ kg/m}^3$) predicted by the axisymmetric model correlates well with the 3D Model, both at 1 μ sec. and 2 μ sec.

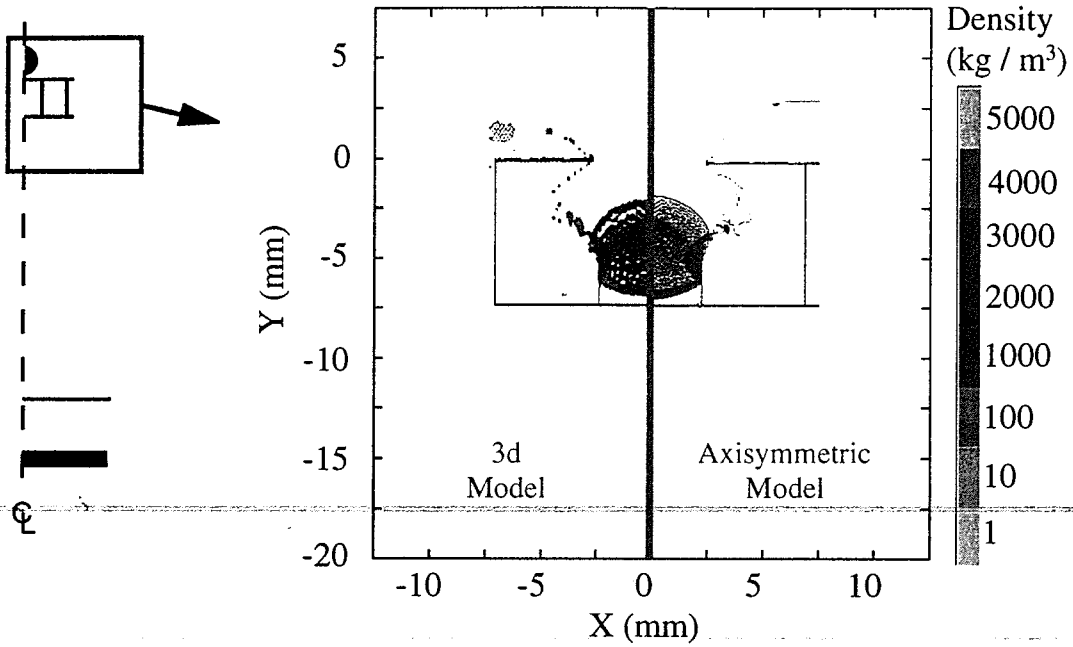


Figure 24. Comparison of 3D and Axisymmetric Predicted Density Distribution at $1 \mu\text{sec}$.

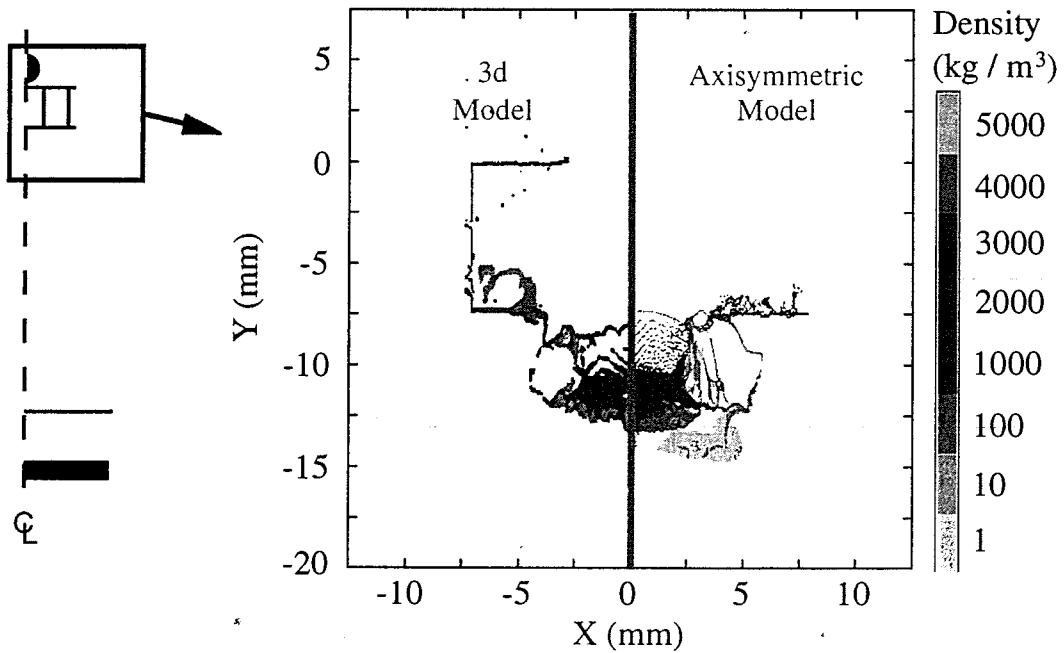


Figure 25. Comparison of 3D and Axisymmetric Predicted Density Distribution at $2 \mu\text{sec}$.

Figures 26 and 27 compare the axial and radial velocity components of the axisymmetric and 3D generated debris clouds. Figure 26 shows the debris cloud in the process of penetrating the honeycomb core layer. Both axial and radial velocity components are similar. Examining the dense central region of the debris cloud, it can be seen that for both models the axial velocity is 6 km/s and the radial expansion velocity is under 0.5 km/s. Some differences are noticeable after the honeycomb core has been penetrated, as shown in Figure 27, however the velocity distribution of the dense central region is still very similar.

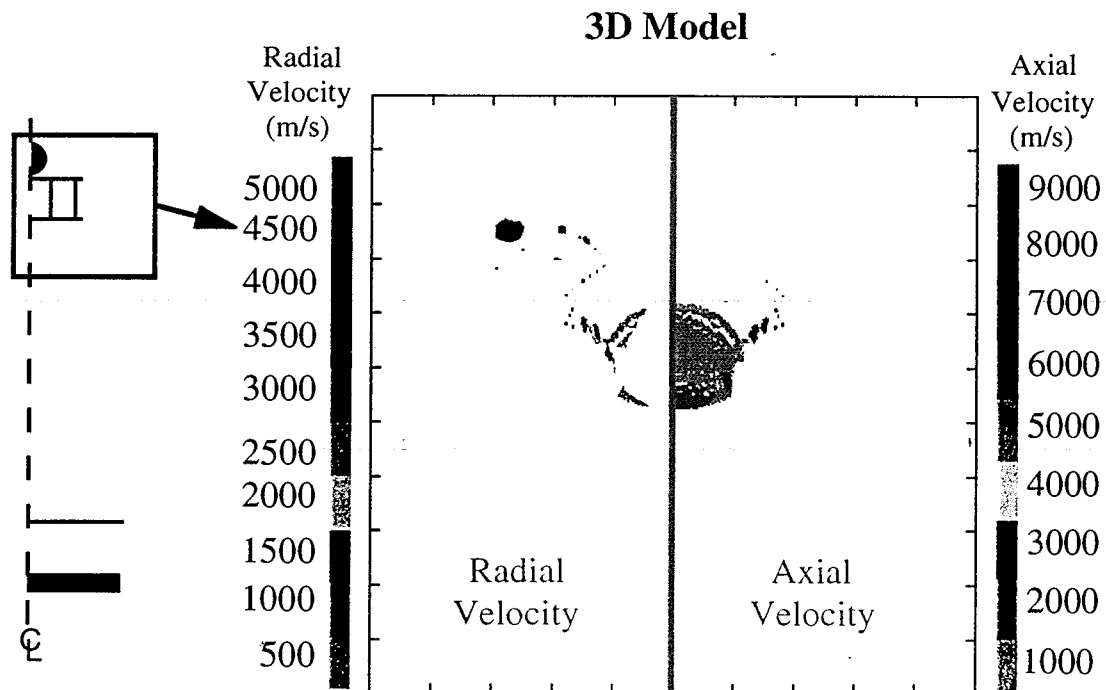
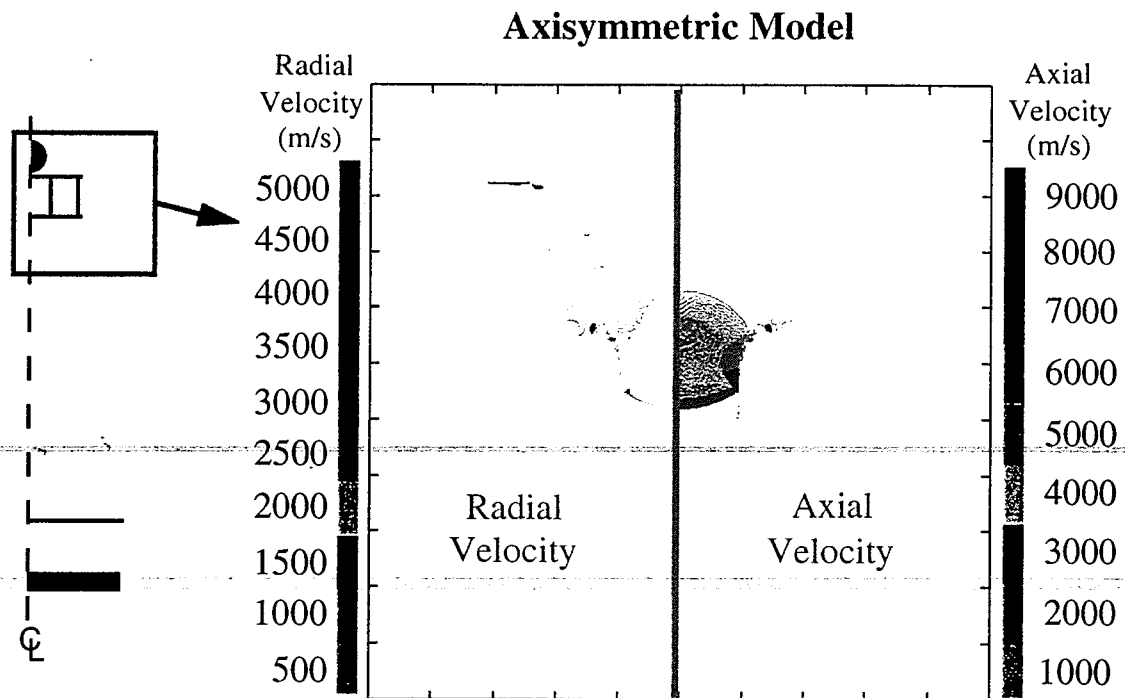


Figure 26. Comparison of Axisymmetric and 3D Predicted Velocity Distributions at 1 μ sec.

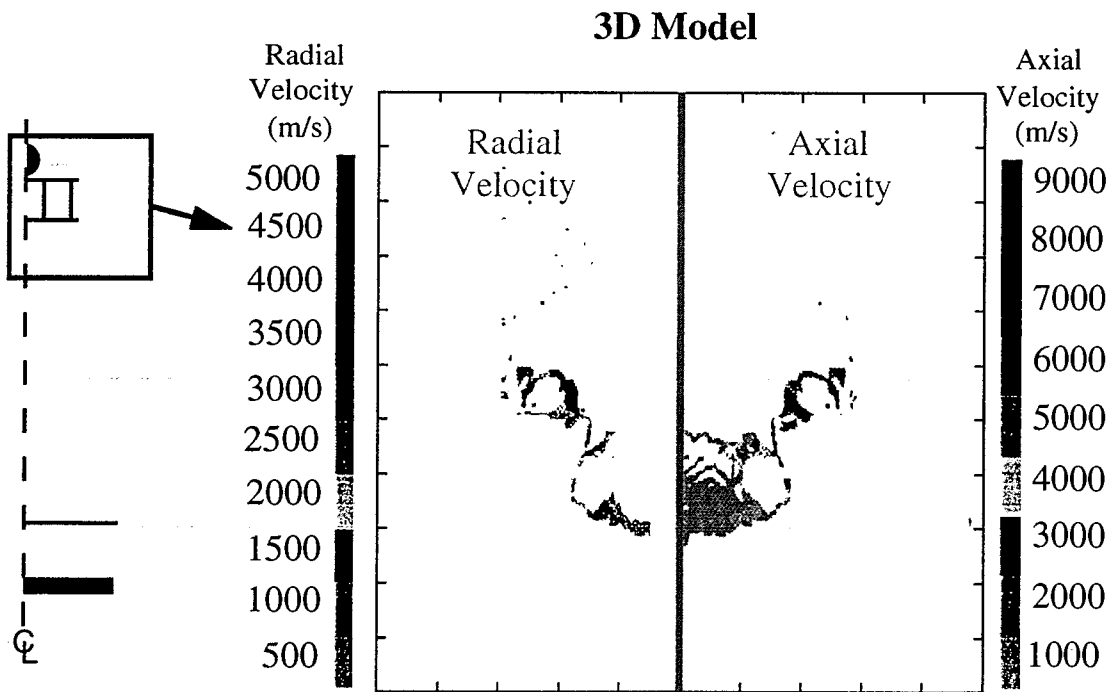
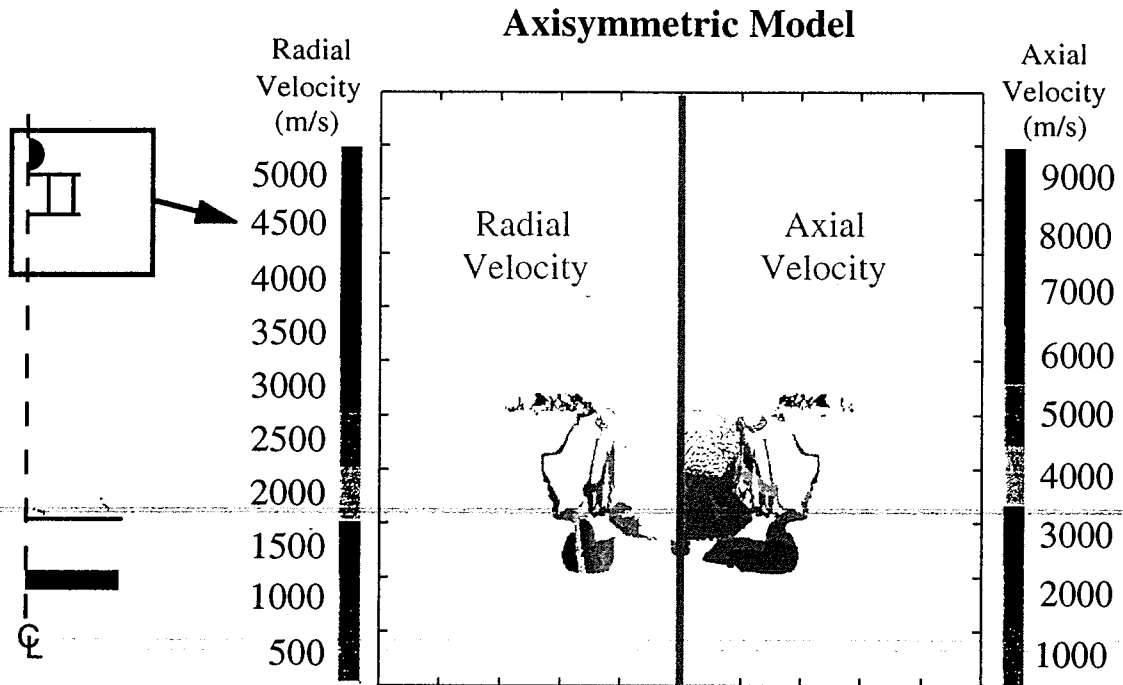


Figure 27. Comparison of Axisymmetric and 3D Predicted Velocity Distributions at 2 μsec.

3.2 Correlation with Experimental Results (Hole Size Comparison)

Table II lists the hole sizes generated both experimentally and numerically. The hypervelocity impact experiment resulted in substructure penetration. It appears that initial impact with the honeycomb layer was neither cell centered or junction centered, but instead an off-centered cell wall junction impact. Petalling occurred on the inner facesheet and accounts for the majority of the recorded hole size. The titanium foil layer, in addition to having a hole form in it, developed an 11 cm tear. The substructure was visibly bulged outward approximately 0.35 cm in the middle of the plate. In addition, craters produced by fragments surround the hole. There is a second substructure hole of dimensions 0.08 cm x 0.04 cm, which was produced by a fragment.

Table II: Hole Size Comparison

Model	Outer Facesheet (cm)	Inner Facesheet (cm)	Titanium Foil (cm)	Sub-structure (cm)
Experiment	0.81	4.88 x 3.38	2.54 x 2.54	0.94x0.43
<i>No H/C Core</i>	0.53	0.9 - 1.44	1.36 - 2.4	1.09 - 1.46
<i>No H/C Core, Titanium Foil Removed</i>	0.53	0.9 - 1.44	N/A	1.47 - 2.13
<i>No H/C Core, Coarse Mesh</i>	0.58	1.24	> 3.00	0.78 - 1.47
<i>Cell Centered Impact</i>	0.52	0.85	1.84	1.16 - 1.49
<i>Junction Centered Impact</i>	0.51	0.98	> 3.00	0.91 - 1.16

Hole sizes generated by CTH are also listed in Table II. Ranges of values are given in cases where it was unclear what value to take for the hole size. Hole sizes listed as > 3.00 cm implies that the entire simulated wall was destroyed. Computed hole sizes for the outer facesheet layer are smaller than the experimental hole size, with the *No H/C Core, Coarse Mesh* Model giving the best comparison to experimental data. A large discrepancy is seen between experimental and computational hole sizes for the inner facesheet layer. This may be due to the inability of axisymmetric models to simulate the tearing and petalling seen

experimentally. In addition, CTH does not have the capability to accurately model material deformations and failures that occur after the initial impact when pressures drop to a lower level. Hole sizes in the titanium foil layer suffer from the same limitations. However, hole sizes in the thicker substructure will be modeled more accurately, because it is not as susceptible to tearing and petalling. Predictions are necessarily limited to the initial microseconds of impact, after which time the accuracy of CTH will decrease. Despite this limitation, predicted hole sizes in the substructure are similar to the experimental hole size (Table II).

Figure 28 compares the damaged region in the experimentally tested substructure to the damage predicted by the *No H/C Core, Coarse Mesh* Model. As can be seen, there is a large 0.94 cm long elliptical hole in the experimental substructure, with a second, smaller hole beneath it. The region between these two holes is severely damaged, with many craters and a large extent of material erosion. Computational results obtained from the *No H/C Core, Coarse Mesh* model are shown to scale with experimental results in the lower half of Figure 28. It can be seen that the *Coarse Mesh* Model compares favorably with experimental results, predicting a hole of 0.78 cm diameter.

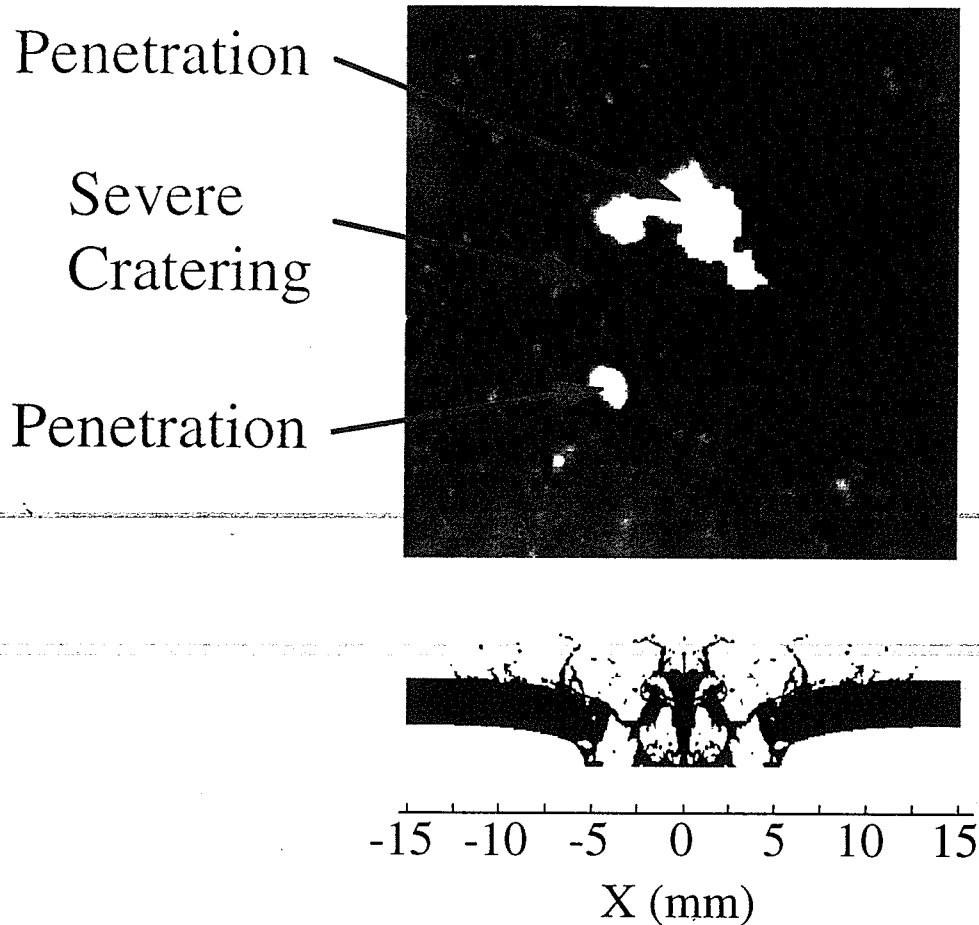


Figure 28. Comparison of Experimental Substructure Damage to *No H/C Core, Coarse Mesh Prediction.*

3.3 Impulse Comparison

In sections 3.1.1 through 3.1.8, results predicted by various models were compared on a qualitative basis. Debris cloud shape and density distributions were studied during penetration of the outer TPS layers, and the predominant damage mechanisms were examined during substructure penetration. A single damage parameter which would allow assessment of the potential for a given debris cloud to penetrate the substructure was desired. This would allow promising TPS configurations to be identified without running the simulation to completion, saving a significant amount of runtime. In addition, identification of a damage parameter would allow direct, quantitative comparison of debris cloud lethality between debris

clouds generated during penetration of different TPS configurations. No single variable was found that would accurately predict debris cloud damage potential. However, peak specific impulse readings were taken in the substructure. In order to take these readings, it is required to run the simulation until the substructure is penetrated, so no time savings are provided as would be if a damage parameter were identified. However, it will be shown that this quantity is related to two of the substructure damage mechanisms predicted computationally. By recording the peak specific substructure impulse a direct, quantitative comparison is possible between different computational models. There are many considerations involved in interpreting the significance of peak specific substructure impulse readings, as will be discussed in this section

In each of the calculations performed, specific impulse (impulse per unit area) readings were taken between 0.006 and 0.036 cm under the impacted surface of a structure. Readings were taken using Lagrangian Tracer Points at discrete points, with the first point located on the axis of symmetry and successive points located radially outward. Lagrangian Tracer Points (tracers) are imbedded in the structure material, and are allowed to move with the material as it fails. Tracers record the state of the computational cell that they are in at discrete time increments. Specific impulse is calculated in CTH by integrating computational cell pressure (recorded by a tracer) through time:

$$\tilde{I} = \int P dt \quad (4)$$

where P represents computational cell pressure. Figure 29 shows the pressure reading through time recorded by the axis of symmetry tracer located in the substructure of the *No H/C Core* Model. Figure 30 shows the calculated specific impulse for that tracer. As can be seen, the specific impulse reaches a maximum value at 12 μ sec., after which time only minor fluctuations are reported. This represents the point at which material at that tracer location has failed and been accelerated to the velocity of the impacting debris cloud. These 'peak' specific impulses were recorded for each tracer point and used as a means of comparing the predictions of the various computational models.

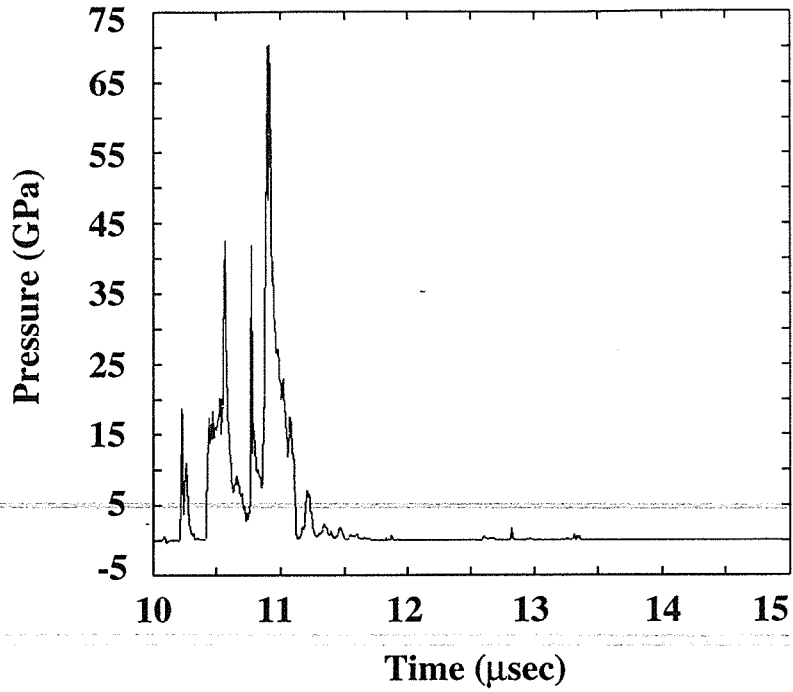


Figure 29. Pressure vs. Time Recorded by Axis of Symmetry Substructure Tracer in No H/C Core Model.

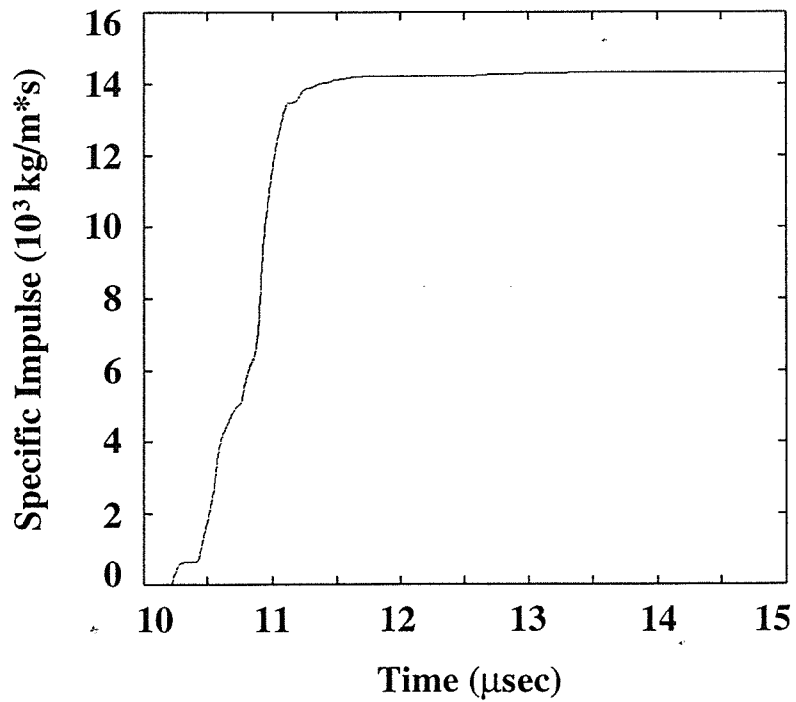


Figure 30. Specific Impulse Calculated from the Pressure Reading in Figure 29.

Peak specific impulse readings should correspond to two of the failure mechanisms witnessed: spalling and momentum failure. Peak specific impulse readings should directly correspond to the level of spalling in the substructure. As previously stated, it is assumed that spalling is due to the impulse generated by the liquid/gaseous portion of the debris cloud. Impulse is defined as:

$$\mathbf{I} = \int \mathbf{F} dt = \int \frac{d\mathbf{p}}{dt} dt = \mathbf{p}_2 - \mathbf{p}_1 = \Delta\mathbf{p} \quad (5)$$

where \mathbf{F} represents the force vector applied to an object, \mathbf{p} represents momentum of the object, and the subscripts 1 and 2 represent state of the object before and after impact. The magnitude of (5) is equivalent to (4) if the force is acting on a unit area. It is thought that peak specific impulse readings should correspond to momentum failure as well. Momentum failure is due to the transfer of momentum from the debris cloud to the substructure. The peak specific substructure impulse is the total momentum per unit area transferred to a point in the substructure. At this point, it is unclear to what extent impulse readings will relate to fragment penetration and cratering damage.

Specific impulse readings will not necessarily relate directly to the pre-impact momentum distribution in the debris cloud. It represents the change in momentum experienced at the point in the impacted structure where the tracer is located. Once that area of the substructure has failed and been accelerated to the speed of the debris cloud, it will cease to be influenced by the debris cloud. In addition, since readings are taken in the impacted structure, momentum multiplication will influence the readings. Despite these complications, the peak specific impulse readings provide quantitative measurements that can be directly compared to the results from other models, and should be related to the probability of spalling and momentum failure occurring in the substructure.

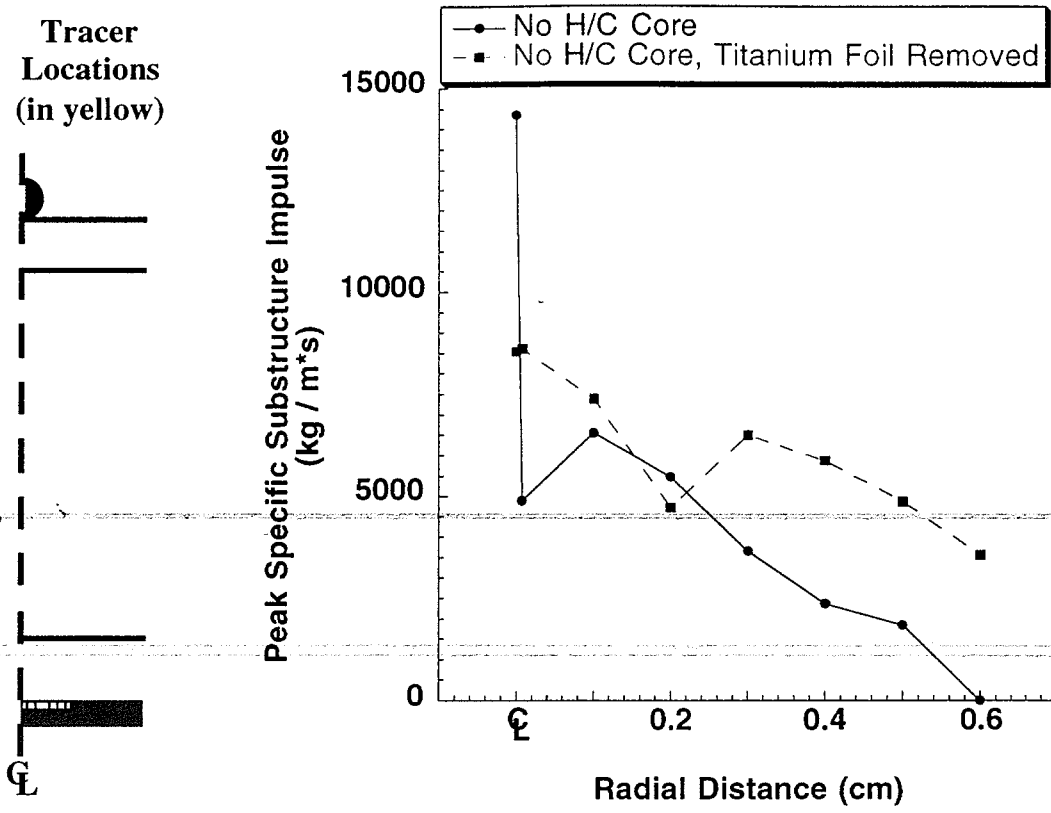


Figure 31. Comparison of Peak Specific Substructure Impulses Generated in No H/C Core and No H/C Core Titanium Foil Removed Models.

Figure 31 compares the substructure impulse for the *No H/C Core* and *No H/C Core, Titanium Foil Removed* Models. The *No H/C Core, Titanium Foil Removed* Model did not experience the level of mass build up along the axis of symmetry that the *No H/C Core* Model did, which explains the lower peak specific impulse reading along the axis of symmetry. In general the peak specific impulse was substantially larger without the titanium foil layer, suggesting that this layer, despite its small thickness, has a large influence on the debris cloud damage potential.

Tracer Locations (in yellow)

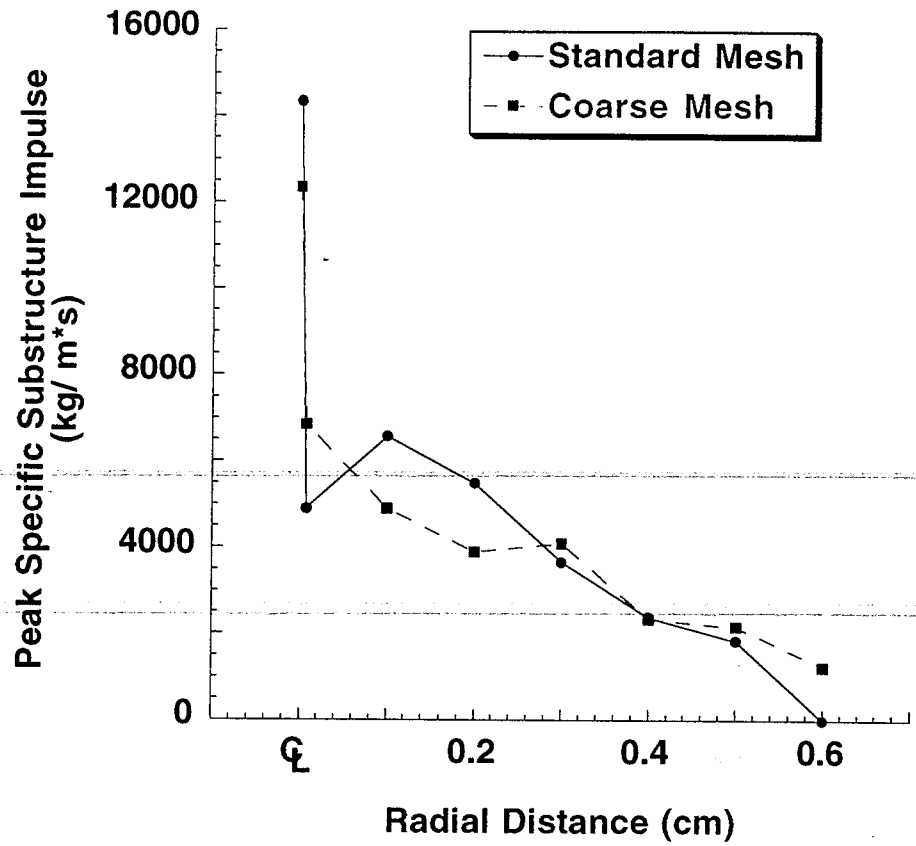
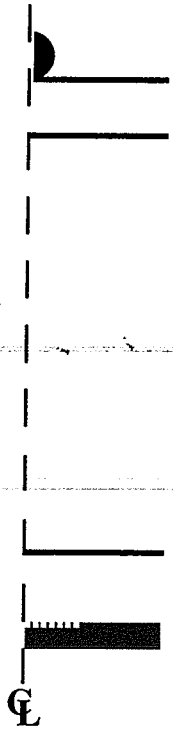


Figure 32. Comparison of Peak Specific Substructure Impulses Generated in *No H/C Core* and *No H/C Core, Coarse Mesh* Models.

Figure 32 compares the *No H/C Core* and *No H/C Core, Coarse Mesh* Models. Using the coarser mesh did not have a pronounced effect on substructure peak specific impulse levels. It can be seen that the two models are very similar at all points.

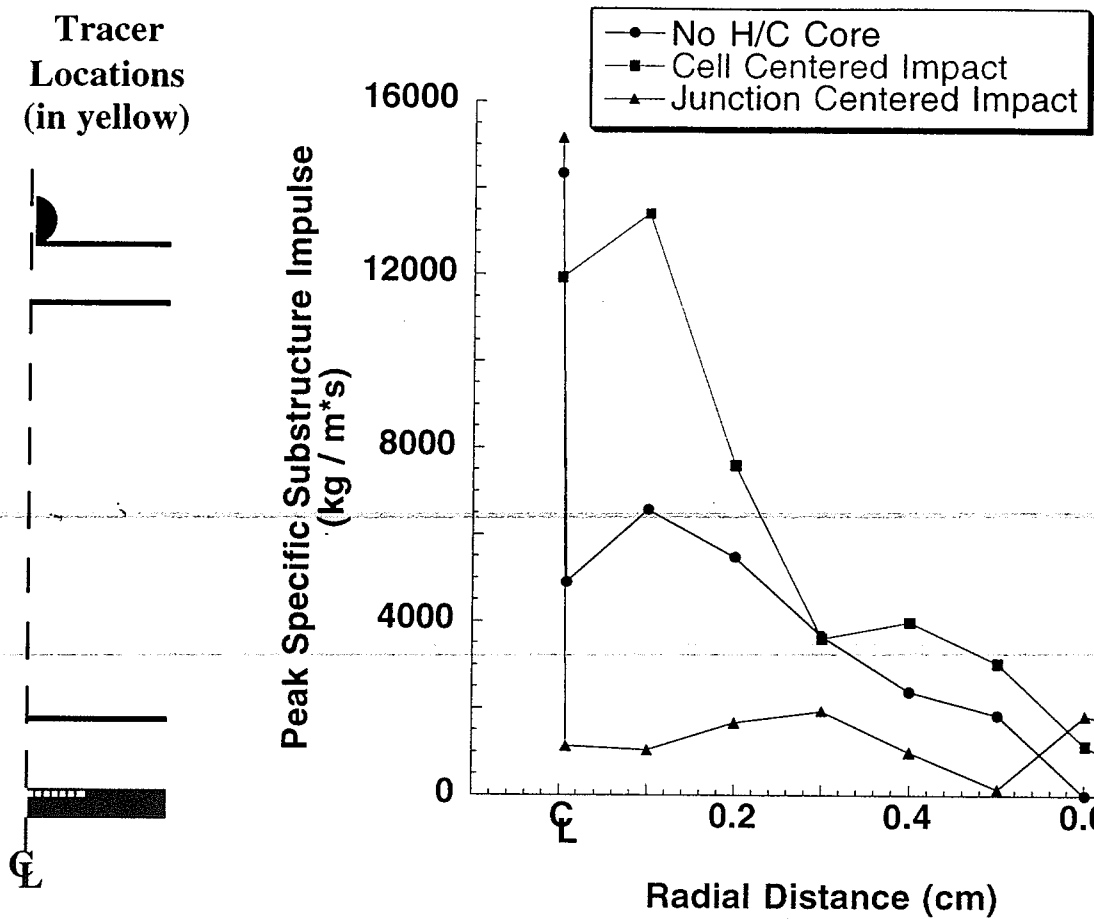


Figure 33. Comparison of Peak Specific Substructure Impulses Generated in No H/C Core, Cell Centered Impact, and Junction Centered Impact Models.

Figure 33 compares the *No H/C Core*, *Cell Centered Impact*, and *Junction Centered Impact* Models to determine the effect of different honeycomb models. Ignoring mass accumulation along the axis of symmetry, the simulated *Cell Centered Impact* produces impulses twice that of the *No H/C Core* Model at radial distances of 0 and 0.1 cm. At all other points the *Cell Centered Impact* Model produced impulses at least equal to the *No H/C Core* Model. The simulated cell junction impact produced impulses much lower than either the *No H/C Core* or *Cell Centered Impact* Models, except at radial distances greater than 0.5 cm. Several factors may contribute to the lower impulse readings. As the projectile impacts the central vertical honeycomb core wall it is deflected radially. A substantial portion of the projectile momentum will be transferred to the massive central rod, causing the rod to move at a

low velocity but drastically reducing axial momentum of the debris cloud. In addition, since the debris cloud is more dispersed after penetrating the honeycomb, it is likely that the titanium foil layer will be more effective at resisting penetration, resulting in the debris cloud which generates a much lower impulse upon impact with the substructure, and therefore possessing less damage potential.

The peak impulses generated during impact were recorded at several discrete points in the outer and inner facesheets of the axisymmetric *Cell Centered Impact* Model and the 3D Model. Figure 34 compares the impulses generated in the outermost facesheet. Peak impulses are seen to be similar, however axisymmetric model generated impulses are as much as 17% higher. There is a more distinct difference in the peak impulses generated in the inner facesheet, as shown in Figure 35. The axisymmetric model predicts a concentration of momentum in the central region of the debris cloud, while the 3D Model predicts a more even distribution of momentum. Impulse measurements are only reported out to the edge of the inner honeycomb core cell wall ($X=0.24$ cm). Significant impulses were not generated outside of the inner cell wall until after the primary debris cloud had completely penetrated the inner facesheet.

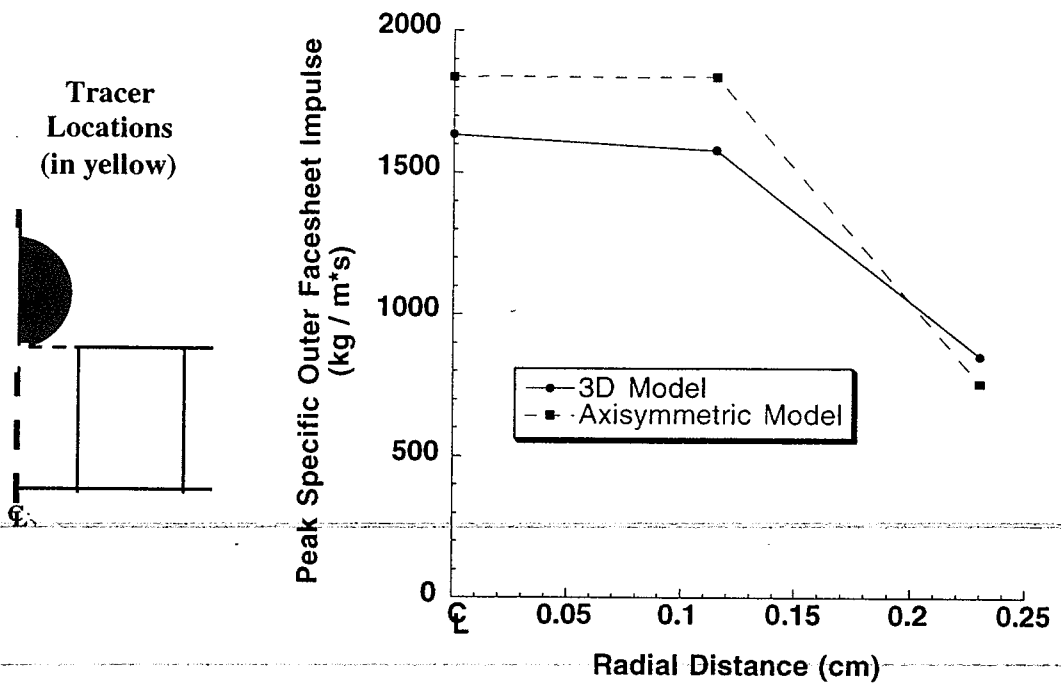


Figure 34. Titanium Peak Specific Outer Facesheet Impulses, Predicted by 3D and Axisymmetric Models.

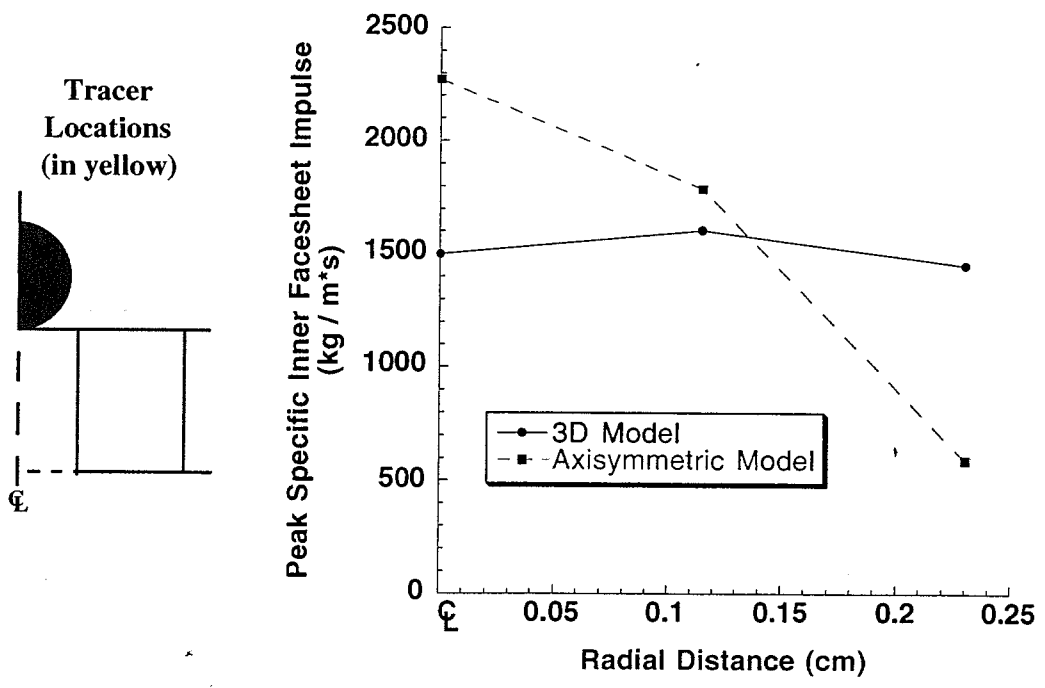


Figure 35. Titanium Peak Specific Inner Facesheet Impulses, Predicted by 3D and Axisymmetric Models.

3.4 Axial Momentum Losses

During the rezoning process, low density material was filtered and material unlikely to influence substructure penetration was removed. Such material includes intact portions of the foil and honeycomb core layers. These layers absorbed debris cloud momentum, but due to their mass were not accelerated to a significant velocity. A specific example is the axisymmetric rod in the *Junction Centered Impact* Model which had a final velocity of 100 m/s due to momentum transfer from the debris cloud. Due to restrictions on computational domain size, it was necessary to discard such material after the initial impact.

Deletion of material during rezones resulted in losses to the overall downward axial momentum, the momentum directed towards the substructure. Substantial reduction of the debris cloud axial momentum may result in an underprediction of substructure damage, the extent of which is unknown. The total downward axial momentum was examined for discontinuities, which would indicate that momentum was lost in a rezone. The magnitudes of these discontinuities were measured and summed to give the total downward axial momentum lost prior to substructure impact. These momentum losses are reported in Table III. In addition, axial momentum was lost in the *No H/C Core* Model when it was necessary to remove the axis of symmetry mass accumulation prior to titanium foil impact. This resulted in a 3% total axial momentum loss, and is included in Table III.

The *Junction Centered Impact* Model used a velocity addition technique, where velocity was subtracted from the computational mesh to render the debris cloud motionless. This substantially reduced the number of rezones required, and no discontinuities were present in the downward axial momentum. It is believed that the primary reason for this is that no low density material filters were required during rezoning. The computation was able to proceed with only the continuously running gas filter, which was set at a level of 0.005 gm/cm³. For this reason, it is thought that the velocity addition technique is more accurate than multiple rezoning.

Table III. Axial Momentum Losses

Model	Momentum Drop (kg*m/s)	% Momentum Drop
No H/C Core	0.22	20.0
<i>No H/C Core, Titanium Foil Removed</i>	0.06	5.5
<i>No H/C Core, Coarse Mesh</i>	0.13	11.8
<i>Cell Centered Impact</i>	0.10	9.1
<i>Junction Centered Impact</i>	0.00	0.0

3.5 Runtime

Runtime was an important consideration, since to run a model to completion often took over a month on the IRIX workstations available. The models were run on several different workstations, requiring that the CPU times be normalized. Table IV lists runtimes in CPU days normalized to represent equivalent runtime on a MIPS R10000 CPU. The runtimes listed represent the best possible runtime, and do not account for inefficiencies that will be encountered, such as rezoning and rerunning, which will easily push the actual simulation time over a month. Removing the titanium foil layer had a significant effect on runtime, resulting in a 56% reduction in runtime from the *No H/C Core* Model. Use of a coarse mesh resulted in the lowest runtime, only 22% of the CPU time required for the *No H/C Core* Model. *Cell Centered Impact* and *Junction Centered Impact* Models increased run time dramatically, due to the small computational cells required to model thin vertical walls.

Table IV: Axisymmetric Model Runtimes

Model	Runtime (CPU days)
No H/C Core	4.62
<i>No H/C Core, Titanium Foil Removed</i>	2.04
<i>No H/C Core, Coarse Mesh</i>	1.03
<i>Cell Centered Impact</i>	10.28
<i>Junction Centered Impact</i>	8.58

4 Conclusions

A series of numerical simulations were performed using the hydrodynamics code CTH to determine an effective way to model the hypervelocity impact of a metallic thermal protection system (TPS). Impact was assumed to occur with a 0.476 cm diameter spherical aluminum particle, impacting normal to the TPS with a velocity of 7.1 km/s. To simplify the problem, impact was modeled in the center region of a TPS panel, away from any fasteners or sidewalls, allowing the problem to be simulated with a two dimensional axisymmetric model consisting of an outer titanium honeycomb sandwich, 5 cm of fibrous insulation, a 0.0076 cm thick titanium foil layer, a 0.95 cm void, and an aluminum substructure of 0.254 cm thickness. This TPS configuration was simulated using seven different axisymmetric models. Three of the models neglected the honeycomb core, one of which used a coarser mesh than standard. Another of the models without honeycomb core neglected the titanium foil layer, to determine if it significantly influenced substructure damage. Two models simulated the honeycomb core using homogeneous layers of reduced density. The density of the homogeneous layer was set equal to the average density of a honeycomb core layer, so that the mass in the path of the incoming projectile would be accurately accounted for. Two other models simulated impact at different points relative to the honeycomb core by using axisymmetric rods and tubes. In all of the models, the fibrous insulation layer was neglected to make the solution feasible. This is not expected to have a significant effect on damage to the substructure, due to the low density of the fibrous insulation layer, and any inaccuracies should be conservative. In addition to axisymmetric models, a single three dimensional model was generated to simulate the impact of a particle directly in the center of a honeycomb core cell. The 3D model exactly models the geometry of the actual structure simulated, and was used to validate the accuracy of the axisymmetric models. In addition, predictions are compared to experimental data.

The 0.076 mm titanium foil layer was found to have a significant influence on the simulation. When removed, the substructure experienced larger peak specific impulses. In addition, the dominant failure mechanism changed, from surface penetration and cratering when the titanium foil was included, to spalling without the titanium foil.

In general, four computational cells were used through wall thicknesses. This was to allow accurate prediction of the shock structure. One model was created which used only two computational cells through a wall thickness. Results were comparable, with both hole sizes and peak specific substructure impulses being similar.

Two of the models simulated the honeycomb core as a homogeneous layer. Neither model produced satisfactory results. Two other models simulated discrete cell walls in the honeycomb core. Simulations of cell centered and cell-wall junction centered impacts, respectively, represented the two extremes of honeycomb core interaction with the projectile. The cell centered model was seen to channel the debris cloud, resulting in substructure impulses much larger than those generated in the model without honeycomb core. The junction centered model had the opposite effect, causing the debris cloud to disperse. Resulting peak specific substructure impulses were much lower than in the model without honeycomb core.

The axisymmetric cell centered model was compared to the 3D Model. Density and velocity distributions were similar for both models. Peak specific impulses were comparable in the outer facesheet, however the axisymmetric model predicted a concentrated impulse in the central region of the inner facesheet where the 3D Model did not. Possibly the most important result of this comparison is the verification of the channeling behavior predicted by the axisymmetric model. Both models predicted that the debris cloud would be contained by the surrounding cell wall during penetration, resulting in a potentially dangerous mass concentration upon exiting the rear of the honeycomb sandwich panel.

Available computers could not simulate the entire TPS configuration at once. Instead, a smaller computational domain was defined around the hypervelocity particle and the outermost TPS layers. As computation proceeded, the computational domain was moved to follow the

impact debris cloud. This was accomplished using two techniques: manual rezoning and velocity addition. Manual rezoning consisted of redefining the computational domain as the debris cloud approached a computational boundary. The second method was to add a uniform velocity field to the computational mesh equal and opposite to the velocity of the debris cloud center of mass. This had the effect of holding the debris cloud stationary in the computational mesh. This method was seen to be more efficient than multiple rezones, and reduced axial momentum losses.

Based on the findings of this analysis, several recommendations can be made for future simulations. It is suggested that future simulations be run with a coarse mesh, running interesting or borderline results with a fine mesh. To design impact protection systems conservatively, the cell centered impact should be modeled. However, if runtime is an issue it may be advisable to use models without a honeycomb layer, running only borderline cases with a cell centered impact. The titanium foil layer was found to be influential and should be included. Finally, velocity addition to the computational mesh should be used in preference to multiple rezoning.

5 References

1. Elfer, N. C., "Structural Damage Prediction and Analysis for Hypervelocity Impacts - Handbook," NASA CR 4706, February, 1996.
2. Blosser, M. L., "Development of Metallic Thermal Protection Systems for the Reusable Launch Vehicle," Presented at the Space Technology and Applications International Forum, 2nd Conference on Next Generation Launch Systems, Albuquerque, NM, 1997. Also published as NASA TM 110296, Oct. 1996.
3. Hertel, E. S., Jr., "Comparison of Analytic Whipple Bumper Shield Ballistic Limits with CTH Simulations," Sandia National Laboratories, SAND92-0347, Albuquerque, New Mexico, 1993.
4. Karr, K. L., Poteet, C. C., Blosser, M. L., "Hypervelocity Impact Test Results for a Metallic Thermal Protection System," NASA TM, publication pending.
5. McGlaun, J. M., et. al., "A Brief Description of the Three-Dimensional Shock Wave Physics Code CTH," Sandia National Laboratories SAND89-0607, July 1990.
6. Anderson, E., Jr., "An Overview of the Theory of Hydrocodes," Int. J. Impact Engng., Vol. 5, pp. 33-59, 1987.
7. Hertel, E. S., Jr., Personal Communication
8. Kerley, G. I., "Theoretical Equations of State for Aluminum," Int. J. Impact Engng. 5, 441-449, 1987.
9. Trucano, T. G. "Library of ANEOS Equations-of-State for CTH," Sandia National Laboratories Report, to be published.
10. Bell, R. L., et. al., "CTH User's Manual and Input Instructions," CTH Development Project, Sandia National Laboratories, Albuquerque, New Mexico, July, 1996.
11. Babcock, S. G., Kumar, A., Green, S. J., "Final Report on Response of Materials to Suddenly Applied Stress Loads. Part I: High Strain-Rate Properties of Eleven Reentry Vehicle Materials at Elevated Temperatures," GM Defense Research Laboratories, Technical Report AFFDL-TR-67-35, Part I, April 1967.
12. Silling, S., "Use of the Johnson-Cook Fracture Model in CTH," Computational Physics and Mechanics Department, Sandia National Laboratories, Albuquerque, New Mexico, 1996.
13. Brown, W. F., Mindlin, H., Yo, C. Y., "Aerospace Structural Metals Handbook, 1994 Edition," Vol. 3, CINDAS / USAF CRDA Handbooks Operation, Purdue University, West Lafayette, IN, 1994.
14. Brown, W. F., Mindlin, H., Yo, C. Y., "Aerospace Structural Metals Handbook, 1994 Edition," Vol. 4, CINDAS / USAF CRDA Handbooks Operation, Purdue University, West Lafayette, IN, 1994.

15. Hertel, E. S., Jr., Chhabildas, L. C., Hill, S. A., "Whipple Bumper Shield Simulations," Shock Compression of Condensed Matter 1991, S. C. Schmidt, R. D. Dick, J. W. Forbes, D. G. Tasker (editors), Elsevier Science Publishers, New York, 1992.
16. Maiden, C. J., et. al., "Thin Sheet Impact," GM Defense Research Laboratories, General Motors Corporation, Santa Barbara, California, Prepared under Contract No. NAS 9-3081, September, 1965.
17. Chhabildas, L. C., et. al., "Whipple Bumper Shield Results and CTH Simulations at Velocities in Excess of 10 km/s," Sandia Report SAND91-2683, Sandia National Laboratories, Albuquerque, New Mexico, August, 1992.
18. Christman, D. R., et. al., "Summary Report: Study of the Phenomena of Hypervelocity Impact," GM Defense Research Laboratories, General Motors Corporation, Santa Barbara, California, Prepared under Contract No. NAS 8-5067, June, 1963.
19. Dienes, J. K., Walsh, J. M., "Theory of Impact: Some General Principles and the Method of Eulerian Codes," High Velocity Impact Phenomena, Ray Kinslow (editor), Academic Press, New York, 1970.

